

Field-free diode effects in one-dimensional superconductor: a complex interplay between Fulde-Ferrell pairing and altermagnetism

SVS Sai Ruthvik¹ and Tanay Nag^{1,*}

¹Department of Physics, BITS Pilani-Hyderabad Campus, Telangana 500078, India

We investigate the emergence of nonreciprocal dissipationless supercurrents in one-dimension manifested through the superconducting diode effect (SDE) and the Josephson diode effect (JDE) in the absence of any external magnetic field, where inversion symmetry (IS) and time-reversal symmetry (TRS) can be intrinsically broken by spin-orbit coupling (SOC), and altermagnetism (AM), respectively. We investigate Ising and Rashba SOC separately in two models where two-component AM, assembled with crystallographic angle, can lead to qualitatively similar indirect band-gap closing and non-reciprocal supercurrent in a Fulde-Ferrell (FF) superconductor. Interestingly, in the absence of the above SOCs, SDE persists and the sign of efficiency can be altered by tuning the angle only. Parallel spin components with complementary momentum functions, ensuring the breaking of IS and TRS, can induce SDE in the presence of FF pairing. Continuing the analysis in the context of JDE, we explore the interplay between SOCs and AM with the *p*-wave and Fulde-Ferrell superconductivity in three different setups. The bulk bands contributes to the non-reciprocity in the case of *p*-wave superconductivity while JDE is dominated by Andreev bound states for FF superconductivity. Importantly, JDE continues to exist due to finite momentum Cooper pair even without AM and SOC unlike the *p*-wave superconductivity. The sign of JD efficiency can be tuned with angle for *p*-wave superconductivity while absence of such sign reversal is a hallmark signature of FF superconductivity. Similar to SDE, parallel spin components in conjunction with *p*-wave superconductivity can lead to JDE that can also be mediated by only FF pairing in the absence of SOC and AM.

I. INTRODUCTION

The superconductivity is an extraordinary phase of matter where many-body quantum effects make the electric current flow without any resistance below a critical temperature. The celebrated Bardeen-Cooper-Schrieffer (BCS) pairing mechanism, accompanied by zero center-of-mass momentum of the Cooper pairs, can explain the perfectly reciprocal i.e., direction-independent behavior of dissipationless supercurrent¹. Recent experimental studies have shown that the non-reciprocity in the supercurrent can lead to a diode effect namely, superconducting diode effect (SDE)²⁻¹⁰. There exist asymmetry between forward and reverse critical currents. In order to understand the above phenomena, the finite center-of-mass momentum of Copper pairs is found to be a key ingredient while this type of unconventional pairing was theoretically predicted by Fulde and Ferrell (FF)¹¹⁻¹⁶. In the presence of Zeeman field and spin-orbit coupling (SOC) the Fermi-surface gets deformed allowing two opposite spins but with unequal momentum to pair up and form FF superconductor¹⁷⁻¹⁹. Interestingly, there have been a significant amount of theoretical endeavour to understand the exotic phenomena of SDE which is primarily mediated by the magnetic field, SOC and FF pairing²⁰⁻³⁶. It is important to note that SOC breaks inversion symmetry (IS) and magnetic field breaks time-reversal symmetry (TRS) leading to magnetochiral asymmetry (MCA) that is required to experience SDE^{30,37-39}. Importantly, the interplay of magnetic field and SOC also leads to topological superconductivity, however, the deformation of the Fermi-surface and gap opening depends

on the mutual orientation between SOC and magnetic field^{17-19,40,41}. Apart from scientific viewpoint, technologically SDE is a promising phenomenon leading to various quantum devices such as SDE rectifier⁴².

Going beyond the non-reciprocity of the bulk supercurrent in SDE, there have been a great attention to study the nonreciprocal behavior of Josephson current where two superconductors having different phases are interfaced together. The experimental emergence of Josephson diode effect (JDE) enriches the field of nonreciprocal transport in superconductors⁴³⁻⁵⁰. Interestingly, JDE along with finite Cooper pair momentum have been simultaneously observed experimentally⁵¹. Theoretical studies indicate towards the fact that the IS and TRS breaking are very important to obtain asymmetry in the current-phase relation yielding non-zero JD efficiency^{50,52-65}. The electron and hole currents differ from each other under IS-breaking while TRS-breaking causes spin-up and spin-down electrons to carry different amount of current. The intrinsic JDE is analyzed in the absence of external magnetic field where finite momentum Cooper pair plays significant role^{23,34,66}. The Andreev bound state (ABS) contribution to Josephson current is also studied in context of JDE^{67,68}. Note that JDE is noticed in Rashba superconductor⁶⁹, topological insulator^{22,70}, Dirac semimetal^{51,71}, topological superconductors^{72,73}. Therefore, SDE and JDE both require MCA while they may have intriguing connection with the topological aspect of the systems.

The magnetism is another example of many-body order which is significantly different from superconductivity. A new magnetic order, altermagnetism (AM)⁷⁴, dis-

tinct from ferromagnetism or anti-ferromagnetism has been recently discovered experimentally^{75–78}. The AM is considered to be originated from non-relativistic SOC origin while relativistic SOC gives rise to Ising and Rashba SOC. AM, breaking TRS without any net magnetization, is an admixture of ferromagnetic and antiferromagnetic order where the Fermi-surface hosts spin-split as well spin-degenerate features simultaneously. There have been a plethora of theoretical studies focusing on this unconventional *d*-wave magnetism^{75,79–85}. The real space rotation combined with translation symmetry protects the spin configuration of AM. Interestingly, AM can naturally replace the role of the Zeeman field and therefore, AM is found to be very instrumental in the context of superconductivity including topological superconductivity^{86–92}, Weyl semimetal⁹³ and other electronic topological systems^{94–96}.

Given the above background, the AM is an immensely important material's property in the context of SDE and JDE. The TRS breaking can be achieved by AM without the application of any external magnetic field. This opens up an exciting field of diode effects namely, field-free SDE^{9,10,97–99} and field-free JDE^{48,49,62,100,101}. The effect of crystallographic angle of an altermagnetic term is also examined to study JDE in the presence of *p*-wave superconductivity in two-dimension (2D)¹⁰². The *p*-wave superconductivity is found to be essential to obtain JDE in one-dimension (1D) as well¹⁰³. On the other hand, two magnetic fields are required for SDE to experience in 1D^{22,104} while AM induces field-free SDE in 2D^{9,105}. Interestingly, exploiting the MCA, one can also investigate the phenomenon of SDE-mediated Josephson transistor¹⁰⁶. Much having been studied individually about SDE and JDE, while the connection between FF pairing, MCA in the case of field-free diode effects are vastly unexplored. Motivated by this, we systematically explore the answers of the following questions by studying field-free SDE and JDE in 1D: Can AM induce SDE in the absence of SOC (Ising/Rashba or both)? What is the role of crystallographic angle in SDE and JDE as such can it alter the sign of the efficiency? How JDE is manifested in the FF superconductor where *p*-wave superconductivity is absent? Can JDE persist in the absence of AM and SOC?

In this paper, we uncover the field-free route to SDE and JDE by using AM, assembled with crystallographic angle, and two types of SOC such that MCA is present in the system. We first start with FF superconductor in the presence of AM, and Ising (Rashba) SOC in Model I (II) to study the SDE. Examining the low-energy BdG Hamiltonian, we find that the indirect band-gap closing with different probe current is connected with the non-reciprocity of the supercurrent with the finite momentum of the FF superconductor. While there exists qualitative similarity in the non-reciprocal behavior of supercurrent, the nature of SOC non-trivially governs the efficiency profile along with the strength and angle of AM. Most

importantly, two-component AM with finite α can generate MCA leading to an induction of SDE even without any SOC in both the models. To be precise, the SDE is mainly driven by parallel spin components with complementary momentum functions in the presence of FF pairing. We continue investigating the role of MCA in JDE where consider *p*-wave and FF superconductivity in setup 1 and 2,3, respectively, along with AM and SOC in the intermediate quantum wire (FF superconductor itself) for setup 1,2 (3). Our finding shows that bulk- (ABS-) contributions to Josephson current is significant to produce non-reciprocal current phase relation in setup 1 (3) while JDE is negligible in setup 2. Beside this, sign of efficiency can be altered (remains unaltered) by the angle of AM in setup 1 (2,3) where *p*-wave (FF) superconductivity is present. The field-free JDE is more efficient in the presence of *p*-wave superconductivity, AM and SOC. Similar to SDE, parallel spin components with complementary momentum functions with *p*-wave superconductivity can yield JDE. Remarkably, the finite momentum in FF superconductivity breaks IS and TRS, resulting in non-zero JD efficiency via MCA even in the absence of AM, SOC and *p*-wave superconductivity.

The paper is organized as follows: In Sec. II, we discuss two different SDE models, methods to compute supercurrent, and diode efficiency, and findings associated with these models. In Sec. III, we demonstrate three setups for Josephson junction, formalism to compute the Josephson current, and diode efficiency, and findings corresponding to these setups. In Sec. IV, we connect the field-free SDE and JDE in terms of the sources of MCA. In Sec. V, we conclude with future directions.

II. SUPERCONDUCTING DIODE EFFECT (SDE)

A. Model and band dispersion

We consider a simple 1D tight-binding model with IS breaking Rashba (Ising) SOC and TRS breaking AM of strengths $\lambda_R(\lambda_I)$ and J_A , respectively⁸³. The normal-state with spinful lattice Hamiltonian is then given by $H_0(\lambda_I, \lambda_R) = \frac{1}{2} \sum_{n=1}^{L-1} \left[t \sum_{\sigma=\uparrow, \downarrow} c_{n,\sigma}^\dagger c_{n+1,\sigma} - i\lambda_I (c_{n,\uparrow}^\dagger c_{n+1,\uparrow} - c_{n,\downarrow}^\dagger c_{n+1,\downarrow}) - i\lambda_R (c_{n,\uparrow}^\dagger c_{n+1,\downarrow} + c_{n,\downarrow}^\dagger c_{n+1,\uparrow}) + J_A [\cos 2\alpha (c_{n,\uparrow}^\dagger c_{n+1,\uparrow} - c_{n,\downarrow}^\dagger c_{n+1,\downarrow}) + i \sin 2\alpha (c_{n,\uparrow}^\dagger c_{n+1,\uparrow} - c_{n,\downarrow}^\dagger c_{n+1,\downarrow})] + \text{h.c.} \right] = \sum_{n,m} \tilde{\Psi}_n^\dagger \tilde{H}_0^{nm}(\lambda_I, \lambda_R) \tilde{\Psi}_m$ where L is the number of lattice sites, t represents the nearest-neighbour hopping. and $\tilde{\Psi}_m = (c_{m,\uparrow}, c_{m,\downarrow})^T$. Here α is the crystallographic angle of the AM¹⁰². Now coming to the superconducting part, the FF pairing is taken as on-site $(\Delta(n)c_{n,\uparrow}^\dagger c_{n,\downarrow}^\dagger + \text{h.c.})$ with a spatially varying order

parameter for the pair-density wave, $\Delta(n) = \Delta e^{iqn}$ where $n = 1, \dots, L$ denotes the site-index. Finally, assembling particle and hole blocks in the Nambu basis $\Psi_n^\dagger = (\tilde{\Psi}_n^\dagger, \tilde{\Psi}_n) = (c_{n\uparrow}^\dagger, c_{n\downarrow}^\dagger, c_{n\uparrow}, c_{n\downarrow})$ on n -th site, one obtains the lattice BdG Hamiltonian

$$H_{\text{BdG}}^{\text{I(II)}}(q) = \begin{pmatrix} \tilde{H}_0^{\text{I(II)}} - \mu I & \hat{\Delta} \\ \hat{\Delta}^\dagger & -\tilde{H}_0^{\text{I(II)*}} + \mu I \end{pmatrix}, \quad (1)$$

which is a $4L \times 4L$ Hermitian matrix. Note that the pairing off-diagonal block in spin space is $\hat{\Delta} = -i\sigma_y \otimes \Delta(n)$ where the diagonal matrix $\Delta(n) = \Delta \text{ diag}\{e^{-iqn}\}$ where Δ denotes the momentum independent superconducting gap amplitude. Here, $\mu I \equiv -\mu \sum_{n,\sigma} c_{n,\sigma}^\dagger c_{n,\sigma}$ with μ being the chemical potential. For our analysis, we take into consideration $\lambda_I \neq 0 = \lambda, \lambda_R = 0$ [$\lambda_I = 0, \lambda_R \neq 0 = \lambda$] in $\tilde{H}_0^{\text{I}}(\lambda, 0)$ [$\tilde{H}_0^{\text{II}}(0, \lambda)$] to construct Model I (II) with BdG Hamiltonian $H_{\text{BdG}}^{\text{I}}(q)$ ($H_{\text{BdG}}^{\text{II}}(q)$).

One can Fourier transform the above BdG Hamiltonian Eq. (1) to obtain the momentum space BdG Hamiltonian in the Nambu basis $\Psi_k = (c_{k+\frac{1}{2}q,\uparrow}, c_{k+\frac{1}{2}q,\downarrow}, c_{-k+\frac{1}{2}q,\uparrow}^\dagger, c_{-k+\frac{1}{2}q,\downarrow}^\dagger)^T$, given by

$$\mathcal{H}_k^{\text{I(II)}}(q, \Delta) = \begin{pmatrix} H_{\text{I(II)}}(k + \frac{1}{2}q) - \mu & -i\sigma_y \Delta \\ i\sigma_y \Delta^* & -H_{\text{I(II)}}^*(-k + \frac{1}{2}q) + \mu \end{pmatrix}. \quad (2)$$

The diagonal kinetic part, which is the Fourier transform of $\tilde{H}_0^{\text{I(II)}}$, depends on the momentum q of the FF pairing and off-diagonal superconductivity is independent of q . In general, the kinetic part is given by

$$H_{\text{I(II)}}(k) = (t \cos k - \mu) \sigma_0 + \lambda \sin k \sigma_\beta + J_A (\cos k \cos 2\alpha + \sin k \sin 2\alpha) \sigma_z. \quad (3)$$

where λ (J_A) identifies the strength of SOC (AM). Here, $\sigma_{x,y,z}$ are the Pauli matrices in spin space, and σ_0 is the 2×2 identity. Importantly, the AM term can be thought of as a dressed AM term $J_A \cos(k - 2\alpha)$ which reduces to conventional AM term in the absence of the crystallographic angle. Finite α produces two-component AM. Note that $\beta = x$ represents the Rashba SOC while $\beta = z$ denotes the Ising SOC. Therefore, we treat Ising case as Model I with BdG Hamiltonian $\mathcal{H}_k^{\text{I}}(q, \Delta)$ and Rashba case as Model II with BdG Hamiltonian $\mathcal{H}_k^{\text{II}}(q, \Delta)$, having kinetic terms as $H_{\text{I}}(k)$ and $H_{\text{II}}(k)$, respectively. We consider hopping t and other parameters in the units of meV.

In the absence of SOC i.e., $\lambda = 0$ and $\alpha = 0$, the normal part $H_{\text{I(II)}}(k)$ preserves IS, generated by $\mathcal{C} = \sigma_z$, such that $\mathcal{C}H_{\text{I(II)}}(k)\mathcal{C}^{-1} = H_{\text{I(II)}}(-k)$. In the absence of AM i.e., $J_A = 0$, $H_{\text{I(II)}}(k)$ preserves TRS $\mathcal{T} = \mathcal{K}\sigma_y$ such that $\mathcal{T}H_{\text{I(II)}}(k)\mathcal{T}^{-1} = H_{\text{I(II)}}(-k)$, \mathcal{K} denotes complex conjugation. We note that $H_{\text{I(II)}}(k)$ breaks IS and TRS when in the presence of SOC $\lambda \neq 0$ and AM $J_A \neq 0$, respectively. It is noteworthy that $\alpha \neq 0$ also

breaks IS even when $\lambda = 0$ when the kinetic Hamiltonian $H_{\text{I(II)}}(k)$ only contains AM. The BdG Hamiltonian with $\lambda = 0, \alpha = 0$ and $q = 0$ preserves IS such that $\tilde{\mathcal{C}}\mathcal{H}_k^{\text{I(II)}}(0, \Delta)\tilde{\mathcal{C}}^{-1} = \mathcal{H}_{-k}^{\text{I(II)}}(0, \Delta)$ with $\tilde{\mathcal{C}} = \mathcal{C}\tau_z$. Importantly, for $q \neq 0$, $\mathcal{H}_k^{\text{I(II)}}(q, \Delta)$ no longer preserves IS even if $\lambda = 0$ and $\alpha = 0$. Now coming to the TRS of BdG Hamiltonian with $J_A = 0$ and $q = 0$, $\tilde{\mathcal{T}} = \mathcal{T}\tau_z$ such that $\tilde{\mathcal{T}}\mathcal{H}_k^{\text{I(II)}}(0, \Delta)\tilde{\mathcal{T}}^{-1} = \mathcal{H}_{-k}^{\text{I(II)}}(0, \Delta)$. Importantly, for $q \neq 0$, $\mathcal{H}_k^{\text{I(II)}}(q, \Delta)$ breaks TRS even if $J_A = 0$. This indicates the fact that finite momentum pairing causes IS and TRS breaking in the superconductor irrespective of SOC and AM. Therefore, finite momentum $q \neq 0$, is a sufficient condition for SDE to occur, while the breaking of IS and TRS in the normal part $H_{\text{I(II)}}(k)$ is a necessary condition. It is important to note that SOC and magnetic field are required to generate finite momentum of the Cooper pair¹⁷. In short, TRS and IS breaking are mandatory conditions to obtain SDE.

As discussed earlier, the non-reciprocity in the critical current is the main essence of SDE. Upon changing the direction of magnetic field or probe current, the critical current also alters in magnitude in addition to its direction. It has been shown that magnetochiral anisotropy is required to obtain SDE^{30,69,98}. In dimension $D \geq 2$, the critical current is given by $j_c(B) = j_c(0)[1 + \tilde{\gamma}(\hat{C} \times \hat{B}) \cdot \hat{J}]$ where \hat{C} denotes the direction of IS breaking, \hat{B} represents the magnetic field which can be in-plane (out-of-plane) if SOC is out-of-plane (in-plane) and \hat{J} is the direction of the probe current. The probe current effectively mimics finite momentum of the Cooper pair. $\tilde{\gamma}$ denotes the strength of magnetochiral anisotropy. Therefore, directions of IS breaking, magnetic field and Cooper pair momentum have to be orthogonal to each other to experience the effect of $\tilde{\gamma}$. The anisotropy in current thus can be examined either by reversing the magnetic field or the probe current such that $\hat{B} \rightarrow -\hat{B}$ ($\hat{J} \rightarrow -\hat{J}$) keeping \hat{J} (\hat{B}) unaltered, leading to $j_c^+ \neq j_c^-$. Note that the Pauli matrices associated with SOC and magnetic field are considered to be the direction of \hat{C} and \hat{B} , respectively, in $D \geq 2$. Interestingly, for our study in $D = 1$, parallel spin matrices corresponding to IS and TRS breaking components contribute to MCA that we explore extensively while studying SDE and JDE.

Here, our aim is to demonstrate SDE in the absence of any external magnetic field, rather in the presence of AM. The AM is associated with σ_z due to its local magnetic moments restricting us from altering its direction unlike the external magnetic field. Given the fact that AM is along the out-of-plane direction, we allow for two different types of SOC, namely in-plane Rashba and out-of-plane Ising SOC, to examine SDE³⁰. It is important to note that in-plane Rashba (out-of-plane Ising) SOC and out-of-plane (in-plane) magnetic field are responsible for observing SDE. We investigate the non-reciprocity in supercurrent by changing the sign of q which is the same as changing the direction of the probe current J .

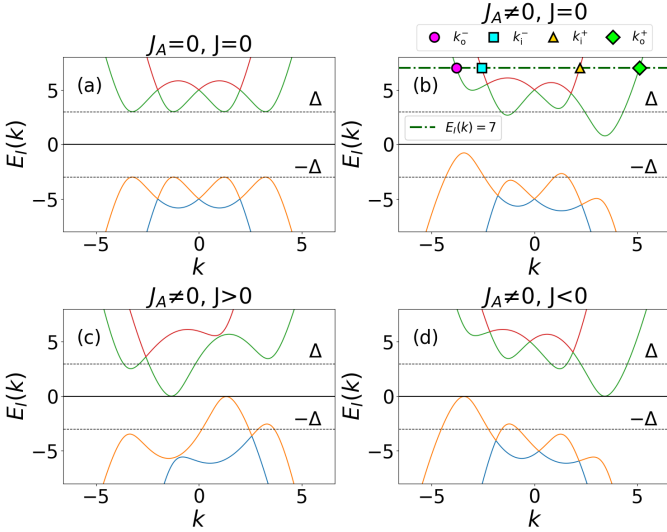


FIG. 1. We show $E_I(k)$, derived from Eq. (2) and (4) for Model I low-energy Hamiltonian, for $(J_A, J) = (0, 0), (0.2, 0), (0.2, 1.18)$, and $(0.2, -0.35)$ in (a), (b), (c), and (d), respectively. The plot (b) depicts the inner and outer circle crossings for $E_I(K) = 7$. For this Ising Case: $k_o^- = -3.796$, $k_i^- = -2.572$, $k_i^+ = +2.199$, $k_o^+ = +5.103$. Parameters: $t = 1$, $\mu = 4$, $\Delta = 3$, $\lambda = 2$, $\alpha = 0$.

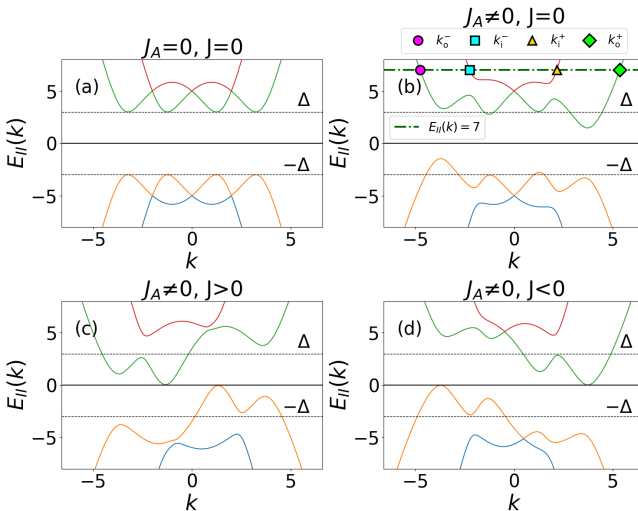


FIG. 2. We show $E_{II}(k)$, derived from Eq. (2) and (4) for Model II low-energy Hamiltonian, for $(J_A, J) = (0, 0), (0.6, 0), (0.6, 1.18)$, and $(0.6, -0.75)$ in (a), (b), (c), and (d), respectively. The plot (b) depicts the inner and outer circle crossings for $E_{II}(K) = 7$. For this Rashba Case: $k_o^- = -4.757$, $k_i^- = -2.247$, $k_i^+ = +2.159$, $k_o^+ = +5.347$. Parameters: $t = 1$, $\mu = 4$, $\Delta = 3$, $\lambda = 2$, $\alpha = 0.125\pi$.

Therefore, we investigate AM-mediated SDE following two routes namely, Model I with Ising SOC and Model II with Rashba SOC.

We now present the low-energy BdG model with $\cos k \approx k^2$ and $\sin k \approx k$ in Eq.(2) yielding the normal

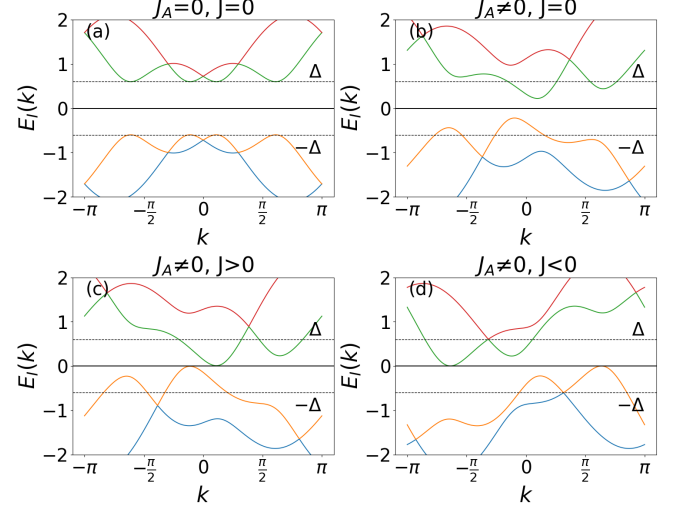


FIG. 3. We show $E_I(k)$, derived from Eq. (2) and (3) for Model I lattice Hamiltonian, for $(J_A, J) = (0, 0), (0.4, 0), (0.4, 0.35)$, and $(0.4, -1.18)$ in (a), (b), (c), and (d), respectively. Parameters: $t = 1$, $\mu = 0.6$, $\Delta = 0.6$, $\lambda = 1$, $\alpha = 0$.

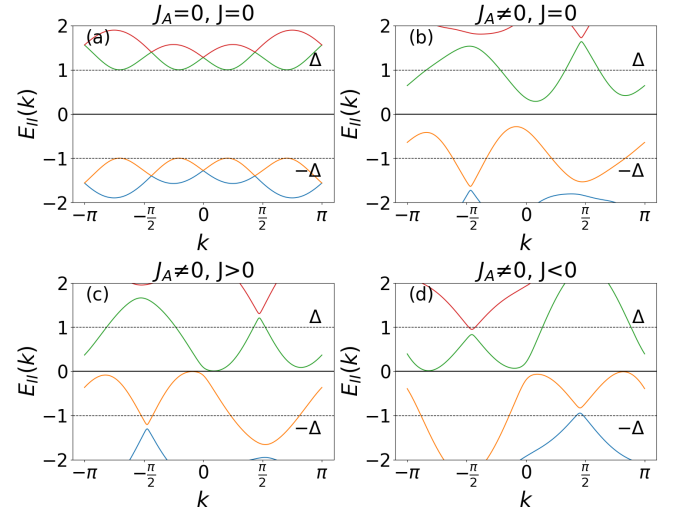


FIG. 4. We show $E_{II}(k)$, derived from Eq. (2) and (3) for Model II lattice Hamiltonian, for $(J_A, J) = (0, 0), (1.3, 0), (1.3, 0.55)$, and $(1.3, -1.95)$ in (a), (b), (c), and (d), respectively. Parameters: $t = 1$, $\mu = 0.2$, $\Delta = 1$, $\lambda = 1$, $\alpha = 0.125\pi$.

part

$$H_{I(II)}(k) \approx (tk^2 - \mu) \sigma_0 + \lambda k \sigma_{z(x)} + J_A (k^2 \cos 2\alpha + k \sin 2\alpha) \sigma_z. \quad (4)$$

The corresponding BdG Hamiltonian Eq. (2) is given by $\mathcal{H}_k^{I(II)}(q, \Delta) \approx (tk^2 - \mu) \sigma_0 \tau_z + \lambda k \sigma_{z(x)} \tau_0 + J_A k^2 \cos(2\alpha) \sigma_z \tau_z + J_A k \sin(2\alpha) \sigma_z \tau_0 + t(q^2/4) \sigma_0 \tau_z + tkq \sigma_0 \tau_0 + \lambda(q/2) \sigma_{z(x)} \tau_z + J_A (q^2/4) \cos(2\alpha) \sigma_z \tau_z + J_A kq \cos(2\alpha) \sigma_z \tau_0 + (q/2) \sin(2\alpha) \sigma_z \tau_z + \Delta \sigma_y \tau_y$.

We now examine the band dispersion from the low-energy model in Fig. 1 for the Model I with Ising SOC. The Ising SOC lifts the degeneracy of the earlier quadratic spin-degenerate bands except at $k = 0$. In the absence of J_A , see Fig. 1 (a), the isotropic nature of the bands is observed with degeneracy at $k = 0$. This results in concentric Fermi surfaces when the Fermi energy is kept above $E_k > 5$. The center of the inner and outer rings overlap at $k = 0$. In the presence of finite $J_A \neq 0$, the Fermi surfaces no longer remain concentric leading to a separation between the centers of inner and outer rings, see Fig. 1 (b). In other words, J_A introduces anisotropy in the dispersion which could potentially lead to coupling between two electrons of opposite spins and opposite but unequal momentum $k_{o,i}^+ \neq k_{o,i}^-$. In the presence of AM, the Fermi surfaces are deformed from their circular structure. Therefore, the deviation of the centers $k_{o,i}^c = (k_{o,i}^+ + k_{o,i}^-)/2$ of inner and outer rings with respect to $k = 0$ can effectively cause a finite Cooper pair momentum q_0 to emerge. k_o^c and k_i^c are of opposite signs. It turns out that the change in the finite momentum, i.e., $\delta q \equiv q - q_0$, due to the passing of a current through the superconductor is proportional to the current⁶⁶. Interestingly, the probe current J directly accounts for q i.e., $J \equiv q$ in the BdG Hamiltonian and hence passing a probing current in the direction of (against) q_0 eventually closes the gap of the inner (outer) pocket, see Figs. 1 (c,d). This gap closing in opposite directions happens at different values of J namely J_{\pm} which signifies the asymmetric nature of the indirect band gap as a function of q with respect to $q = 0$. This directly indicates that the superconducting gap vanishes asymmetrically with $J \equiv q$ causing different critical currents in opposite directions. Therefore, the superconducting diode effect takes place as long as $J_+ \neq J_-$ or $q_+ \neq q_-$ features are evident from band dispersion^{20,22}.

We examine the dispersion of the low-energy version of Model II with Rashba SOC in Figs. 2 (a,b,c,d) where we qualitatively find identical features as those of Model I. In the presence of J_A , the inner and outer Fermi surfaces no longer remain concentric. Under positive and negative probe currents, the band gaps of inner and outer surfaces close at different values of J suggesting the emergence of SDE. To take this a step further, we study the dispersion of the tight-binding version of Model I and II in Figs. 3 and 4, respectively. The asymmetric behavior of the indirect band-gap closing is a key signature of the upcoming SDE. Therefore, the AM substantiates the role of an external magnetic field when there exists SOC. Having analyzed the band dispersion, we now proceed with the formulation of SDE in the next section.

B. Formulation of SDE

We now discuss the framework to compute the supercurrent. There exist two methods, one is using the

condensation energy in momentum space and other one is based on the current operator formalism in real space. These formalisms apply to both the models with BdG Hamiltonian $\mathcal{H}_{I(II)}$ in momentum and real spaces. We only follow the condensation energy formalism for our analysis of SDE. We first demonstrate the momentum space formalism where we evaluate the derivative of the condensation energy density with respect to the FF pairing momentum q .

The BdG Hamiltonian $\mathcal{H}_k^{I(II)}(q, \Delta)$ is diagonalised on a discrete momentum grid, and the free energy density is obtained as^{22,107,108}

$$\Omega_{I(II)}(\Delta, q) = -\frac{1}{L} \sum_{k, \eta=\pm} \frac{1}{\beta} \ln \left[\cosh \left(\frac{\beta E_{\eta, k, q}^{I(II)}}{2} \right) \right], \quad (5)$$

where the index η labels two branches of the spectrum i.e., valence and conduction bands with $E_{\eta, k, q}^{I(II)}$ being the positive eigenvalues of $\mathcal{H}_k^{I(II)}(q, \Delta)$. $\beta = 1/T$ is the inverse temperature, and L is the length of the nanowire or the number of k points used for Brillouin-zone sampling $k = 2\pi n/L$ with $n = 1, \dots, L$. Hence, the condensation energy density is given by $F_{I(II)}(\Delta, q) = \Omega_{I(II)}(\Delta, q) - \Omega_{I(II)}(0, q)$. The supercurrent is then obtained from the derivative of the free energy²⁰

$$j_{I(II)}(q) = 2e \frac{\partial F_{I(II)}(\Delta, q)}{\partial q}, \quad (6)$$

where e is the electron charge. The extrema of the current, j_{\max} and j_{\min} yield the superconducting diode coefficient, quantifying the degree of non-reciprocity, defined as

$$\gamma_{I(II)} = \frac{j_{I(II)}^{\max} - |j_{I(II)}^{\min}|}{j_{I(II)}^{\max} + |j_{I(II)}^{\min}|}. \quad (7)$$

This procedure allows us to determine both the current-momentum relation $j_{I(II)}(q)$ and the degree of nonreciprocal response γ with the above prescription.

A current operator formalism is followed to compute the total current using the real-space BdG Hamiltonian $\mathcal{H}_{BdG}^{I(II)}(q)$ in Eq. (1). The charge current operator in real space is obtained from the hopping terms in the tight-binding form

$$\hat{J}_{I(II)} = ie \sum_{n,m} \Psi_n^\dagger T_{nm}^{I(II)} \Psi_m, \quad (8)$$

where $T_{nm}^{I(II)} = (1/2)(t[\delta_{n,m+1} + \delta_{n+1,m}] \sigma_0 \tau_z - i\lambda(\delta_{n,m+1} - \delta_{n+1,m}) \sigma_z (x) \tau_0 + \bar{J}_A [\cos 2\alpha(\delta_{n,m+1} + \delta_{n+1,m}) + i \sin 2\alpha(\delta_{n,m+1} - \delta_{n+1,m})] \sigma_z \tau_z)$ is the hopping matrix of size $4N \times 4N$ appearing in the BdG Hamiltonian. The expectation value of the BdG current operator over occu-

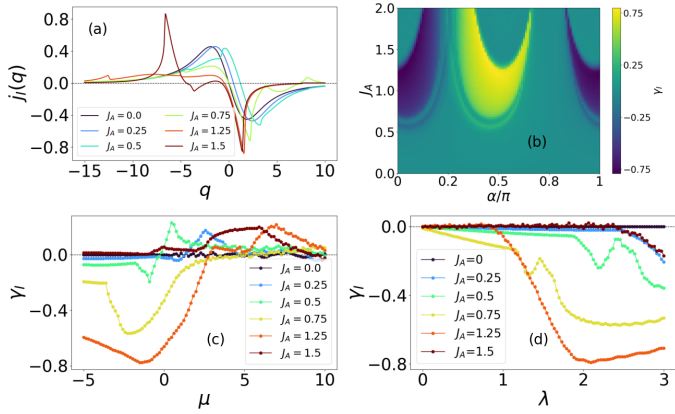


FIG. 5. In (a), we show the variation of supercurrent $j_I(q)$, derived from Eqs. (5), (6) for Model I low-energy Hamiltonian, with the finite momentum of the Cooper pair. In (b), we illustrate the heat-map of γ_I derived from Eq. (7) as a function of angle α , and amplitude J_A of altermagnet term. In (c,d), we display the variation of SD efficiency with μ and Ising SOC λ , respectively. We consider $\mu = -1.52$ for (a),(b) and (d). We choose $\lambda = 1.97$ for (a),(b) and (c). We choose $\alpha = 0.017\pi$ for (a),(c) and (d). Parameters: $t = 1$, $\Delta = 2.02$, $\beta = 10000$.

plied quasiparticle states yields the supercurrent $j_{I(II)}(q)$,

$$j_{I(II)}(q) = \frac{1}{N} \sum_{E_n^{I(II)} < 0} \langle u_n^{I(II)} | \hat{J}_{I(II)} | u_n^{I(II)} \rangle f(E_n^{I(II)}) \\ = \frac{1}{N} \text{Tr}[(U_{\text{occ}}^{I(II)})^\dagger \hat{J}_{I(II)} U_{\text{occ}}^{I(II)} F], \quad (9)$$

where $f(E_n^{I(II)}) = (1 + \exp(-\beta E_n^{I(II)}))^{-1}$ is the Fermi-Dirac distribution with Fermi-energy $E_F^{I(II)} = 0$ and F is a diagonal matrix with elements as $f(E_n^{I(II)})$. $|u_n^{I(II)}\rangle$ are eigenvectors of $H_{\text{BdG}}^{I(II)}(q)$ Eq. (1), associated with eigenvalue $E_n^{I(II)}$, and $U_{\text{occ}}^{I(II)}$ collects the occupied eigenvectors as columns composing a matrix of $4N \times 2N$. The definition of efficiency Eq. (7) is independent of the method adopted to compute supercurrent. In the case of tight-binding models, we note that $j_{I(II)}(q)$, computed using momentum space, yields the same results as obtained from the real space lattice model. In the case of low-energy model, one can only adopt the condensation energy formalism to estimate the supercurrent.

C. Results

In this section, we present the key outcomes of our numerical analysis on the current and the diode efficiency. We examine two distinct scenarios: the Ising case and the Rashba case namely, Model I and Model II using Eq. (2), respectively. For each scenario, we perform calculations using both the low-energy model and the full

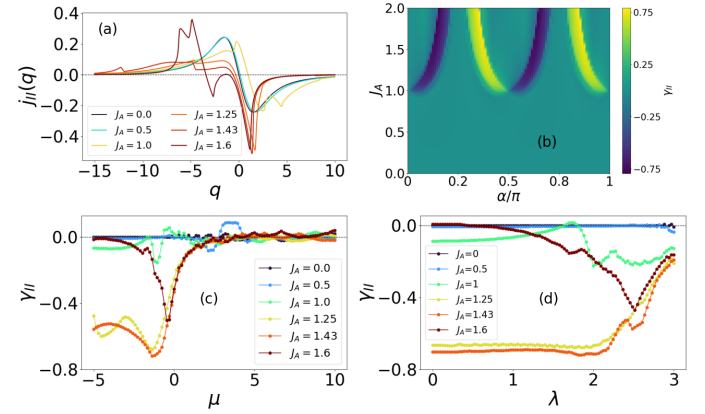


FIG. 6. In (a), we show the variation of supercurrent $j_{II}(q)$, derived from Eqs. (5), (6) for Model II low-energy Hamiltonian, with the finite momentum of the Cooper pair. In (b), we illustrate the heat-map of γ_{II} derived from Eq. (7) as a function of angle α , and amplitude J_A of altermagnet term. In (c,d), we display the variation of SD efficiency with μ and Rashba SOC λ , respectively. We consider $\mu = -1.36$ for (a),(b) and (d). We choose $\lambda = 1.87$ for (a),(b) and (c). We choose $\alpha = 0.111\pi$ for (a),(c) and (d). Parameters: $t = 1$, $\Delta = 1.21$, $\beta = 10000$.

tight-binding Hamiltonian. A comparative discussion of these results is provided below.

We now examine the variation of the supercurrent $j_{I(II)}(q)$, computed using Eq. (6), with FF momentum q for Model I and II in Figs. 5 (a) and 6 (a), respectively. We find that supercurrent passes through $q = 0$ for $J_A = 0$ in both the models and the momentum q_* at which supercurrent vanishes $j(q_*) = 0$ acquires more positive values as J_A increases till a threshold value. Till this threshold value, $j_{I(II)}(q)$ does not show much asymmetry in terms of its positive and negative values. Above this value, for example, $J_A > 0.5$ (1.0) for Model I (II), q_* suddenly becomes negative and supercurrent shows significant asymmetry in terms of its positive and negative values. This is maximized for $J_A = 1.25$ (1.43) in Model I (II), as seen from Figs. 5 (a) and 6 (a) where the positive supercurrent is markedly smaller as compared to the negative counterpart. Note that supercurrent switches its sign just once till the maximum non-reciprocity arises. Therefore, there exists an optimum choice of J_A for both the models for which the efficiency is maximized. After the above values of J_A , supercurrent displays multiple crossings over q axis leading to multiple sign reversals of the supercurrent which can be considered as a signature of AM domination. Therefore, the AM strength can be tuned to maximize the diode efficiency resembling the magnetic field variation. The supercurrent approaches zero when q is large indicating the suppression of superconductivity. The current-momentum behavior of both the models is qualitatively similar except for the quantitative value of J_A at which the efficiency is maximum.

We now study the SD efficiency γ Eq. (7) over J_A - α plane for Model I and II in Figs. 5 (b) and 6 (b), respectively. The behavior of γ between $\pi < \alpha < 2\pi$ is same as that of between $0 < \alpha < \pi$. The periodicity is π as the AM term contains $\sin 2\alpha$ and $\cos 2\alpha$. Interestingly, the sign of efficiency can be reversed by tuning α which does not have any analog as far as the external magnetic field is concerned. As anticipated, γ varies periodically with α , having a period of π . One observation is that the $\gamma = 0$ is always true at $\alpha = \pi/4$ and $\alpha = 3\pi/4$, and the diode efficiency is anti-symmetric about these two points between $0 \rightarrow \pi/2$ and $\pi/2 \rightarrow \pi$ respectively. In Model I, the efficiency acquires a finite value for smaller AM strength as compared to Model II. For $\alpha = n\pi$, $(n+1/2)\pi$ with $n = 0, 1, \dots$, the SD efficiency varies from zero to a maximum value within a window of J_A in Model I. This feature is completely absent in Model II where efficiency is always zero irrespective of the choice of J_A . Importantly, the sign of γ changes around $\alpha = (2n+1)\pi/4$ [$\alpha = n\pi/2$] and with $n = 0, 1, \dots$ in Model I [II]. These features are caused by the underlying nature of the SOC whether it is Ising type or Rashba type. The band of J_A within which γ is finite, depends on α in Model I while in Model II the band of J_A is almost insensitive to α except for around $\alpha = n\pi/2$.

We now examine the evolution of γ with chemical potential μ in Figs. 5 (c) and 6 (c), respectively for Model I and II. The efficiency is insignificant as long as q_* is positive in Figs. 5 (a) and 6 (a). As soon as q_* becomes negative, the efficiency acquires finite values at $\mu = 0$. Interestingly, the magnitude of γ increases as μ approaches zero from negative side for both the models. For Model II, the efficiency reduces and vanishes when μ increases on the positive side. This behavior is not observed in Model I where efficiency can change its sign. Therefore, the nature of the SOC also dictate the behavior with μ . However, in both the models, efficiency follows a qualitatively similar trend for negative μ values.

At the end, we here examine the variation of efficiency with SOC strength in Figs. 5 (d) and 6 (d) for Model I and II, respectively. Remarkably, we find that for different values of α , γ vanishes without Ising SOC in Model I while it remains finite without Rashba SOC in Model II. This reinforces the fact that non-zero α breaks IS even without SOC. This IS breaking together with TRS breaking due finite J_A cause the SDE to appear. For negative q_* in Fig. 5 (a), we find that the magnitude of γ increases with Ising SOC strength λ followed by a decrease in Model I. On the other hand, for Model II, efficiency associated with negative q_* stays almost constant till a certain value of Rashba SOC strength after which its magnitude decreases. Therefore, there exists an optimum choice of λ for both the models for which the efficiency is maximized.

It is important to note that the efficiency reaches a maximum value of ≈ 0.78 in both the models justifying the use of AM instead of an external magnetic field. In

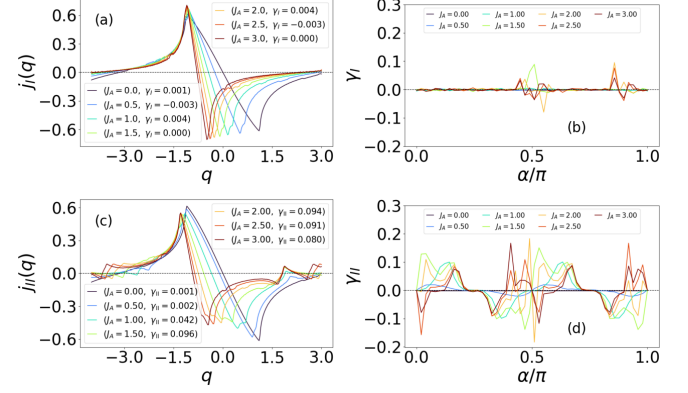


FIG. 7. We show supercurrent variation with FF pairing momentum in (a) and SD efficiency versus α in (b) for Model I lattice Hamiltonian. We repeat (a,b) for Model II lattice Hamiltonian in (c,d), respectively. We consider $\alpha = 0.162\pi$ for (a) and (c). Parameters: $t = 1$, $\mu = 0.6$, $\Delta = 0.682$, $\lambda = 1$, $\beta = 10000$.

our models, the IS is still broken due to SOC even at $\alpha = 0$, the AM perfectly replaces the Zeeman field to break the TRS. An important outcome is that, unlike previous observations in the case of Zeeman field with perpendicular spin component²², the two-component AM with parallel spin component is found to produce the diode effect. A single component of AM can still produce nonreciprocity when another parallel component arises from the Ising SOC. Instead of having SOCs, we made use of the finite crystal angle $\alpha \neq 0$, yielding two-component AM, to observe the changes in diode efficiency.

Having investigated the SDE results in low-energy models, we now work with the lattice models to compute the supercurrent following the condensation energy formalism Eq. (6) what we did for the low-energy model. We demonstrate the current-momentum behaviour in Fig. 7 (a) and Fig. 7 (c) for Models I and II, respectively. We find that the supercurrent vanishes at $q = 0$ when $J_A = 0$. Interestingly, in both models, q_* shifts continuously towards more negative values as J_A increases. This shift slows down for higher values of J_A . The supercurrent vanishes for $q \rightarrow \pm\pi$ indicating the breakdown of superconductivity for larger values of q . The variation of γ with crystallographic angle α for the lattice model shows qualitatively similar features as that of the low-energy model, i.e., γ vanishes at $\alpha = 0, \pi/4, \pi/2, 3\pi/4$ and π . We demonstrate the above variation for Models I and II in Fig. 7 (b) and Fig. 7 (d), respectively, for better representation. The sign of efficiency can be altered with α . The SD efficiency γ is extremely small for Model I, while for Model II it attains a maximum magnitude of ≈ 0.18 . Model II exhibits noticeable variation of γ with α than that of Model I. On the other hand, Model I and II both exhibit high enough efficiency while studying using their low-energy models. In the lattice versions, one can do self-consistent calculations which may lead to al-

most similar efficiencies. However, the predictions from the low-energy models are qualitatively validated in the lattice models as far as the qualitative features are concerned.

We now revert to the efficiency analysis for the low-energy version of the models, as the efficiency is significantly less for the lattice version of the models. We discuss the behavior of γ over λ - α plane for Model I with Ising SOC and Model II with Rashba SOC, respectively, in Fig. 8 (a) and Fig. 8 (b). For $\alpha = 0$, one can find SDE in Model I with Ising SOC while SDE no longer exists in Model II with Rashba SOC. There exists a critical strength of Ising SOC above which SDE is experienced for $\alpha = 0$. On the other hand, for $\lambda = 0$, SD efficiency acquires finite value for certain window of α around $\alpha \approx (2n + 1)\pi/8$ with $n = 0, 1, \dots$. Therefore, crystallographic angle α can break IS and leads to SDE even in the absence of Ising and Rashba SOC. For a given $\alpha \approx 5\pi/8 \neq 0$, the sign of efficiency can be altered with Ising SOC while for Rashba SOC such sign reversal is not possible. For $\lambda = 0$, under identical conditions as expected, SDE is obtained for the same windows of α in both the models. Interestingly, the window of α within which efficiency is finite grows with λ in Model I justifying critical strength of Ising SOC. This behavior is not observed in Model II where such a window of α slowly vanishes above a certain value of Rashba SOC. Therefore, Ising SOC and Rashba SOC both produce SDE with different characteristic features. This proves that AM with the help of the crystallographic angle α , can astonishingly replace both the Zeeman field and the SOC to break TRS and IS simultaneously.

We now explore the $\alpha = 0$ characteristics of γ in more detail. For $\alpha = 0$, the two-component AM reduces to a single-component AM. We find that there exists no SDE for $\alpha = 0$ in Model II which is markedly different as compared to Model I. This is indeed remarkable in the sense that perpendicular spin components i.e., σ_x in Rashba SOC and σ_z in a single-component AM, do not contribute to SDE irrespective of the strength of Rashba SOC. By contrast, the parallel spin components i.e., σ_z in Ising SOC and σ_z in a single-component AM, can produce SDE after a threshold value of Ising SOC. This is a remarkable finding for the 1D field-free SDE while the field-induced SDE requires perpendicular magnetic fields²². Importantly, the complementary momentum functions are needed for the parallel spin components to produce SDE in 1D. This is also evident for $\lambda = 0$ case where $\alpha \neq 0$ gives rise to parallel spin component with complementary momentum functions. To strengthen the above inference, we present a case with the combination of both Ising and Rashba SOC in Fig. 8 (c). In this case, the qualitative features of γ is almost the same as Model I as the parallel spin components are always present. As discussed in Sec. II A, the parallel spin components break IS and TRS causing the SDE to appear.

III. JOSEPHSON DIODE EFFECT (JDE)

Having studied the AM-mediated SDE, we now focus on the JDE where the Josephson current behaves in an asymmetric manner with the phase difference between the two superconductors. We describe below the AM models to engineer JDE.

A. Model

In this section, we analyse three distinct setups to investigate the emergence of the JDE. Specifically, Setup 1 consists of two superconductors, hosting both *s*-wave and *p*-wave gaps, coupled through a quantum wire having SOC and AM. Setup 2 involves two FF superconductors connected via a quantum wire having SOC and AM. Setup 3 comprises two superconductors and intermediate quantum wire where one superconductor is with FF pairing, SOC and AM, quantum wire hosts only hopping, while the other superconductor only has *s*-wave pairing.

In order to represent the above three Josephson junction setups concisely, at the beginning we write the lattice Hamiltonian in Nambu/ BdG form. With the Nambu spinor $\Psi_n^\dagger = (c_{n\uparrow}^\dagger, c_{n\downarrow}^\dagger, c_{n\uparrow}, c_{n\downarrow})$, the Hamiltonian reads

$$\mathcal{H}_J = \frac{1}{2} \sum_{n,m} \Psi_n^\dagger H_J^{nm} \Psi_m, \quad H_J = \begin{pmatrix} H_N - \mu I & -i\Delta\sigma_y \\ i\Delta^*\sigma_y & -H_N^* + \mu I \end{pmatrix}. \quad (10)$$

The length of the total 1D wire is L . The left (right) superconductor has length $L_{l(r)}$. The quantum wire has length L_{qw} such that $L = L_l + L_{qw} + L_r$. Here the normal such as particle block is decomposed as $H_N = H_t + H_{\text{SOC}} + H_{\text{AM}}$ where H_t denotes the hopping term. The *s* [*p*]-wave pairing block as $\Delta_s(n_1, n_2, \phi) = \Delta'_s \exp(i\phi) \sum_{n,m=n_1}^{n_2} \delta_{n,m} \sigma_0$ [$\Delta_p(n_1, n_2, \phi) = i\Delta'_p \exp(i\phi) \sum_{n,m=n_1}^{n_2-1} (\delta_{n,m+1} - \delta_{n+1,m}) \sigma_x$] where $\Delta'_{s[p]}$ indicates the *s* [*p*]-wave superconducting gap, ϕ refers to the phase of the gap; $n_{1(2)}$ denotes the first and last site in the segment of interest. In the case of FF superconductor $\Delta(q, n_1, n_2, \phi) = \Delta'_s \exp(i\phi) \sum_{n,m=n_1}^{n_2} e^{iqn} \delta_{n,m} \sigma_0$. μ refers to the chemical potential that can be different for superconductors and the quantum wire while $\mu I(n_1, n_2) = \sum_{n,m=n_1}^{n_2} \delta_{n,m} \sigma_0$. For Ising (Rashba) SOC, $H_{\text{SOC}}^{\text{I(II)}}(n_1, n_2) = -\frac{i\lambda}{2} \sum_{n,m=n_1}^{n_2-1} (\delta_{n,m+1} - \delta_{n+1,m}) \sigma_z$. $H_{\text{AM}}(n_1, n_2) = J_A \sum_{n,m=n_1}^{n_2-1} [\cos 2\alpha(\delta_{n,m+1} + \delta_{n+1,m}) + \sin 2\alpha(i\delta_{n,m+1} - i\delta_{n+1,m})] \sigma_z$. Note that H_t is present everywhere in the whole 1D wire irrespective of superconductivity, SOC and AM, given by $H_t(1, L) = -t \sum_{n,m=1}^{L-1} (\delta_{n,m+1} + \delta_{n+1,m}) \sigma_0$.

The H_{SOC} and H_{AM} are present in the intermediate quantum wire (left superconductor) only for setup 1 and 2 (3). The superconductivity $\Delta = \Delta_s \sigma_0 + \Delta_p \sigma_x$

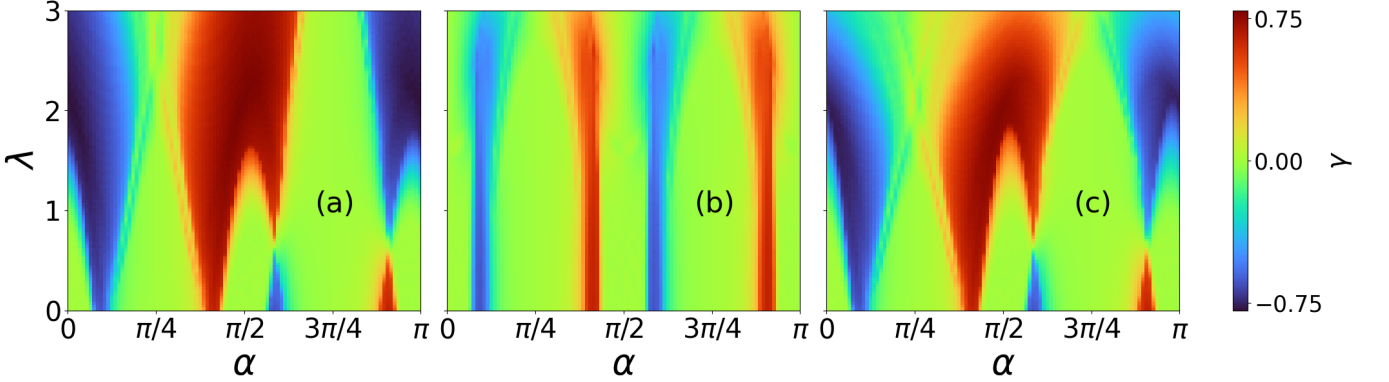


FIG. 8. We show the variation of efficiency over the α - λ plane for low-energy version of Model I in (a). We repeat (a) for Model II in (b). We also repeat the same in (c) with a combination of Ising and Rashba SOC term $\lambda k(\sigma_z + \sigma_x)$ in the Hamiltonian. Parameters: $t = 1$, $\mu = -1.52$, $\Delta = 2.02$, $J_A = 1.22$ and $\beta = 10000$.

($\Delta = \Delta_n(q)\sigma_0$) is present only in setup 1 (2 and 3). Note that Ising (Rashba) SOC yields $H_N^{I(II)}$. We adopt a generic representation of Josephson junction Hamiltonian $H_{J,x}^y$, following Eq. (10), where $y = 1, 2, 3$ denote the setup and $x = I, II$ stands for model. We below demonstrate the Hamiltonian associated with them explicitly. We consider hopping t and other parameters in the units of meV.

Setup 1: The normal part of the Hamiltonian is given by $H_N^{I(II)} = H_t(1, L) + H_{\text{SOC}}^{I(II)}(L_l + 1, L_l + L_{qw}) + H_{\text{AM}}(L_l + 1, L_l + L_{qw})$. The chemical potential is given by $\mu I \equiv \mu_s I(1, L_l) + \mu_0 I(L_l + 1, L_l + L_{qw}) + \mu_s I(L_l + L_{qw} + 1, L)$. The superconductivity is given by $\Delta = \Delta_s(1, L_l, \phi) + \Delta_p(1, L_l, \phi) + \Delta_s(L_l + L_{qw} + 1, L, 0) + \Delta_p(L_l + L_{qw} + 1, L, 0)$. As understood, two different SOC would lead to two different Josephson junction Hamiltonian Eq. (10) for the whole composite chain represented by Hamiltonian $H_{J,I(II)}^1$. Note that a similar model has been studied earlier without AM but with external magnetic field¹⁰³. The setup 1 would explore the effect of AM on JDE in the presence of various SOCs.

Setup 2: In this setup, the normal part and chemical potential of the Hamiltonian are the same as those of setup 1. The superconductors are in FF state and superconductivity is given by $\Delta = \Delta(q, 1, L_l, \phi) + \Delta(2q, L_l + L_{qw} + 1, L, 0)$. Likewise setup 1, two different SOC would lead to two different Josephson junction Hamiltonian Eq. (10) for the whole composite chain represented by Hamiltonian $H_{J,I(II)}^2$. The setup 2 allows us to investigate the effect of finite momentum Cooper pair on JDE in addition to the AM and SOCs which are present in the intermediate quantum wire. Therefore, whether ingredients causing SDE can generate JDE is studied in setup 2.

Setup 3: This setup is an admixture of setup 1 and 2. In particular, the effect of quantum wire is incorporated in the left superconductor which hosts AM

and SOC along with FF pairing and there is no p -wave superconductivity. The quantum wire does not have SOC and AM in it. It only contains hopping. Meanwhile, the right superconductor only has s -wave pairing. The normal part of the Hamiltonian is given by $H_N^{I(II)} = H_t(1, L) + H_{\text{SOC}}^{I(II)}(1, L_l) + H_{\text{AM}}(1, L_l)$. The chemical potential is given by $\mu I \equiv \mu_s I(1, L_l) + \mu_0 I(L_l + 1, L_l + L_{qw}) + \mu_s I(L_l + L_{qw} + 1, L)$. The superconductivity is given by $\Delta = \Delta(q, 1, L_l, \phi) + \Delta_s(L_l + L_{qw} + 1, L, 0)$. Likewise setup 1, two different SOC would lead to two different Josephson junction Hamiltonian Eq. (10) for the whole composite chain represented by Hamiltonian $H_{J,I(II)}^3$. The setup 3 enables us to examine the role of AM and SOC, being present in the FF superconductor itself, on the JDE without any p -wave superconductivity. Therefore, similar to setup 2, we aim here in setup 3 to generate JDE with the help of the ingredients that are essential to cause SDE. To be precise, the left superconductor produces SDE as discussed in the previous Sec. II.

B. Formulation of JDE

In this section, we demonstrate the formalism to compute the Josephson current. The total supercurrent through the junction as a function of superconducting phase difference ϕ is calculated using the expectation value of the current operator in the many-body ground state of BdG Hamiltonian Eq. (10). The current operator \hat{J} is constructed to measure the supercurrent flow, summing over spins, specifically at the bond connecting the superconducting region and the quantum wire/other superconducting region, reflecting the local particle transfer across the interface. It is defined as

$$\hat{J} = ite \sum_{\sigma} \left(c_{n+1,\sigma}^\dagger c_{n,\sigma} - c_{n,\sigma}^\dagger c_{n+1,\sigma} \right), \quad (11)$$

where n denotes the site at the interface i.e., $n = L_l \in$ left superconductor and $n + 1 \equiv L_l + 1 \in$ quantum wire for all setups. The current operator matrix \hat{J} in the BdG framework is constructed in the Nambu basis to facilitate the particle-hole degree of freedom. It takes the form

$$\hat{J}_{\text{BdG}} = \begin{pmatrix} \hat{J} & 0 \\ 0 & -\hat{J}^* \end{pmatrix}. \quad (12)$$

Note that unlike the case of SDE, the current operator here has a contribution coming only from the hopping term only which takes care of the interface current. On the other hand, the bulk supercurrent contributes to SDE.

Now coming to the BdG Hamiltonian H_J of the complete setups Eq. (10), one can obtain the eigenstates $|\psi_n(\phi_l, \phi_r)\rangle$ with eigenvalues $E_n(\phi_l, \phi_r)$ associated with the above Hamiltonian; note that left (right) superconductor has phase $\phi_l = \phi$ ($\phi_r = 0$) associated with the gap functions. Therefore, $\phi_l - \phi_r = \phi$ denotes the net phase difference between left and right superconducting gap functions. The total Josephson current with phase difference ϕ is then evaluated by

$$J_{\text{total}}(\phi) = \frac{1}{et} \sum_{E_n(\phi, 0) < 0} \langle \psi_n(\phi, 0) | \hat{J}_{\text{BdG}} | \psi_n(\phi, 0) \rangle f(E_n), \quad (13)$$

where the sum is taken over all occupied states below fermi energy $E_F = 0$ and $f(E_n) = (1 + \exp(-\beta E_n(\phi, 0)))^{-1}$ denotes the Fermi-Dirac distribution providing a weight factor associated with each energy level. For ease of notation, considering three setup with two models, we designate $J_{\text{total}}(\phi)$ as $J_{x_{\text{total}}}^y(\phi)$ with $y = 1, 2, 3$ for the setups and $x = \text{I}, \text{II}$ for the models. To resolve microscopic contributions, the total current is decomposed into two parts corresponding to two different summations associated with two distinct energy regimes relative to the superconducting gap Δ'_s as follows

$$\begin{aligned} J_{\text{quasi}}(\phi) &= \frac{1}{et} \sum_{E_n < -\Delta'_s/2} \langle \psi_n(\phi, 0) | \hat{J}_{\text{BdG}} | \psi_n(\phi, 0) \rangle f(E_n), \\ J_{\text{ABS}}(\phi) &= \frac{1}{et} \sum_{-\Delta'_s/2 \leq E_n < 0} \langle \psi_n(\phi, 0) | \hat{J}_{\text{BdG}} | \psi_n(\phi, 0) \rangle f(E_n), \end{aligned} \quad (14)$$

with the total current given by $J_{\text{total}}(\phi) = J_{\text{quasi}}(\phi) + J_{\text{ABS}}(\phi)$. The quasi [ABS] current $J_{\text{quasi}}(\phi)$ [$J_{\text{ABS}}(\phi)$] measures the intraband bulk [interband within the superconducting gap] contributions to Josephson current.

The efficiency of the Josephson diode effect is then calculated, which is once again like in Eq. (7), quantified by the nonreciprocity parameter^{109,110}

$$\gamma_x^y = \frac{J_{x_{\text{total}}}^{y, \text{max}} - |J_{x_{\text{total}}}^{y, \text{min}}|}{J_{x_{\text{total}}}^{y, \text{max}} + |J_{x_{\text{total}}}^{y, \text{min}}|}, \quad (15)$$

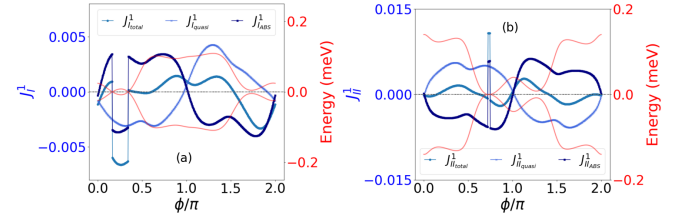


FIG. 9. We show the variation of supercurrent $J_I^1 \equiv J_{\text{quasi}}^1, J_{\text{ABS}}^1, J_{\text{total}}^1$ derived from Eqs. (13) and (14), and energy, with the superconducting phase difference (ϕ) for setup 1 Model I in (a). We repeat the same for setup 1 Model II in (b). We consider $J_A = 4.4444$ for (a) and $J_A = 0.6465$ for (b). Parameters: $t = 40$ meV, $\mu_s = \mu_0 = -1.875t$, $\Delta'_s = 0.0125t$, $\lambda = 0.04t$, $\Delta'_p = 9.828\Delta'_s$, $\alpha = 0.36\pi$, $L_l = L_r = L_{qw} = 20$.

where $J_{x_{\text{total}}}^{y, \text{max}}$ and $J_{x_{\text{total}}}^{y, \text{min}}$ denote the maximum forward and reverse total Josephson currents $J_{x_{\text{total}}}^y(\phi)$ over the phase period. Here, $y = 1, 2, 3$ denotes three setup and $x = \text{I}, \text{II}$ refers to the Model I and II given the setup. This metric captures the rectification efficiency of the junction. Note that in setups 2 and 3, we choose a particular value of q to analyze the JD efficiency.

Alternatively, the Josephson current, flowing across the junction in the presence of phase bias ϕ , can be alternatively computed using the following prescription

$$J_{\text{total}}(\phi) = \sum_{E_n(\phi, 0) < 0} \frac{\partial E_n(\phi, 0)}{\partial \phi} f(E_n) \quad (16)$$

The summation over energy levels can be decomposed $E_n < -\Delta'_s/2$ and $-\Delta'_s/2 \leq E_n < 0$, to obtain J_{quasi} and J_{ABS} , respectively. We follow both the approaches given in Eqs. (13), (16) to compute the Josephson current and its quasi and ABS contributions. The above correlation persists irrespective of the length of the quantum wire and ABS contribution, however, such a correlation breaks once the p -wave superconductivity is present. Note that, we consider $T = 0$ such that $f(E_n) = 1$ for all our calculations. We follow Eqs. (13) and (14) to compute the Josephson current for all our following calculations.

C. Results

In the following sections, we discuss the major outcomes and takeaways from the three setups with underlying Ising SOC and Rashba SOC for Model I and II, respectively in multiple parametric regimes. We examine the total Josephson current into two parts namely quasi- and ABS- contributions to the total current. At the outset, we note that the breaking of IS and TRS is important to observe JDE as well. Therefore, MCA is important to produce JDE, however, finite momentum pairing is not thought to be an important ingredient to

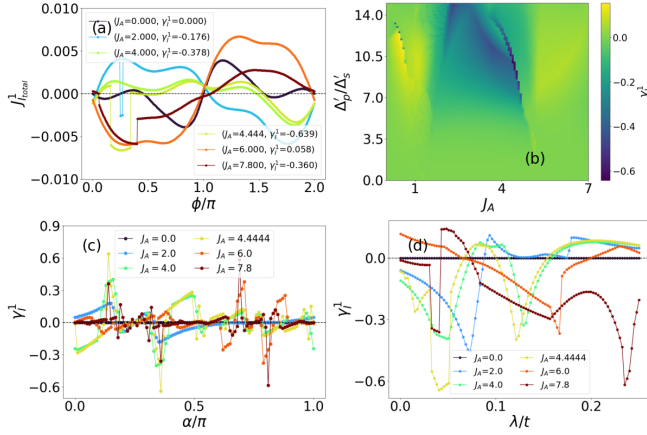


FIG. 10. In (a), we show the variation of supercurrent J_{total}^1 , derived from Eq. (13) for setup 1 Model I, with the superconducting phase difference (ϕ). In (b), we illustrate the heatmap of γ_1^1 derived from Eq. (15) as a function of altermagnet amplitude J_A , and the ratio of triplet and singlet pairing amplitudes (Δ'_p/Δ'_s). In (c,d), we display the variation of JD efficiency with α and Ising SOC λ , respectively. We consider $\lambda = 0.04t$ for (a), (b) and (c). We choose $\Delta'_p = 9.828\Delta'_s$ for (a), (c) and (d). We choose $\alpha = 0.36\pi$ for (a), (b) and (d). Parameters: $t = 40$ meV, $\mu_s = \mu_0 = -1.875t$, $\Delta'_s = 0.0125t$, $L_l = L_r = L_{qw} = 20$.

experience JDE unlike SDE. Below we will explore all setup and examine the role of MCA along with finite momentum pairing. Importantly, the magnetic field is replaced with AM causing the MCA to appear which plays an important role in JDE.

Setup 1: We first examine the setup with Model I in Fig. 9 (a) where we show CPR $J_I^1 \equiv J_{I_{\text{quasi}}}^1, J_{I_{\text{ABS}}}^1, J_{I_{\text{total}}}^1$ (left axis) along with the dispersion (right axis) of the lowest conduction and the highest valence bands. The dispersion inside the superconducting gap shows crossing which corresponds to discontinuous profile of J_{ABS} . This is caused by the change in chirality between two bands during the crossing. Importantly, the bulk contributions J_{quasi} show smooth continuous behavior due to the gapped nature of the bulk bands. Adding both of them up yields the total Josephson current J_{total} that shows discontinuity when chirality of bands inside the superconducting gap is exchanged during the crossing. Interestingly, there exist asymmetries in the quasi and ABS contributions leading to a substantial non-reciprocity in the CPR for $J_{I_{\text{total}}}^1$ which results in JDE. These jumps in the current cause unusual critical current values in one of the directions carrying the signature of JDE. The bulk contribution can be thought of as a consequence of MCA where intraband physics is important while the ABS contributions are governed by interband physics. Therefore, the non-reciprocity in $J_{I_{\text{total}}}^1$ is caused by MCA and ABS.

We repeat the above analysis for Model II $J_{II}^1 \equiv J_{II_{\text{quasi}}}^1, J_{II_{\text{ABS}}}^1, J_{II_{\text{total}}}^1$ in Fig. 9 (b) where ABS contributions show strong non-reciprocity as compared to quasi

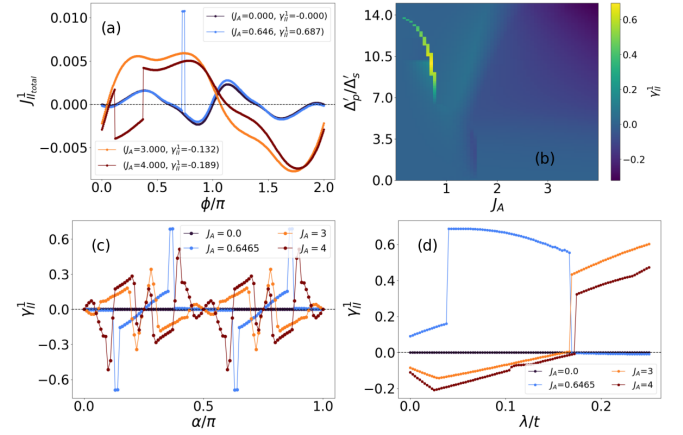


FIG. 11. In (a), we show the variation of supercurrent $J_{II_{\text{total}}}^1$, derived from Eq. (13) for setup 1 Model II, with the superconducting phase difference (ϕ). In (b), we illustrate the heatmap of γ_1^1 derived from Eq. (15) as a function of altermagnet amplitude J_A , and the ratio of triplet and singlet pairing amplitudes (Δ'_p/Δ'_s). In (c,d), we display the variation of JD efficiency with α and Rashba SOC λ , respectively. We consider $\lambda = 0.04t$ for (a), (b) and (c). We choose $\Delta'_p = 9.828\Delta'_s$ for (a), (c) and (d). We choose $\alpha = 0.36\pi$ for (a), (b) and (d). Parameters: $t = 40$ meV, $\mu_s = \mu_0 = -1.875t$, $\Delta'_s = 0.0125t$, $L_l = L_r = L_{qw} = 20$.

contribution. The energy crossings lead to a discontinuity in the ABS contribution indicating the fact that JDE is significantly influenced by ABS rather than MCA. We find qualitatively similar behavior of J_{II}^1 as compared to J_I^1 . Comparing Josephson current for Model I and II in setup 1, we find that non-reciprocity in $J_{I,II_{\text{total}}}^1$ is primarily caused by ABS while MCA contributions are more for Ising SOC than Rashba SOC.

We now move on to the variation of total Josephson current J_{total}^1 with AM strength J_A , crystallographic angle α , and SOC strength λ for Model I and II in Figs. 10 and 11, respectively. It can be seen in Fig. 10 (a) that there exist no non-reciprocity for $J_A = 0$ while ABS and MCA cause the main non-reciprocity for different non-zero values of J_A . Therefore, MCA and ABS both play significant role in producing JDE for Model I. We find that triplet p -wave pairing Δ_p is very crucial to obtain finite JD efficiency γ_1^1 as shown in Fig. 10 (b). The efficiency γ_1^1 is maximized for a certain range of J_A and Δ'_p . The sign of efficiency changes with J_A . We investigate the variation of γ_1^1 with α in Fig. 10 (c) where intermediate (high) values J_A are found to be more relevant to produce JDE around $\alpha = 0, \pi/8, 3\pi/8$, and $\pi/2$ ($5\pi/8$, and $7\pi/8$). Interestingly, $\alpha = \pi/4$, and $3\pi/4$, the efficiency vanishes which resembles the SDE behavior. Importantly, for $\alpha = 0$, a single-component AM can generate JDE in the presence of Ising SOC and p -wave superconductivity. We show the variation of efficiency with Ising SOC strength λ in Fig. 10 (d) where we find JDE does not exist for $J_A = 0$ and $\lambda = 0$ suggesting the importance

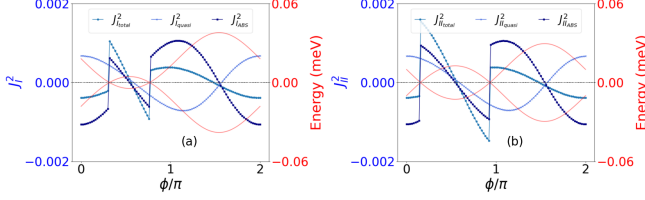


FIG. 12. We show the variation of supercurrent $J_I^2 \equiv J_{I_{\text{quasi}}}^2, J_{I_{\text{ABS}}}^2, J_{I_{\text{total}}}^2$ derived from Eqs. (13) and (14), and energy, with the superconducting phase difference (ϕ) for setup 2 Model I in (a). We repeat the same for setup 2 Model II in (b). Parameters: $t = 40 \text{ meV}$, $\mu_s = \mu_0 = -1.875t$, $\Delta_s = 0.0125t$, $\lambda = 0.05t$, $J_A = 0.5$, $\alpha = 0$, $q = 0.22$, $L_l = L_r = L_{qw} = 20$.

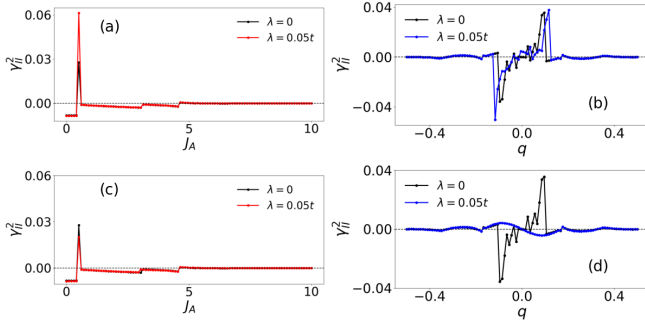


FIG. 13. In (a,b), we show the variation of JD efficiency γ_I^2 , derived from Eq. (15) for setup 2 Model I, with altermagnet amplitude J_A and finite momentum of Cooper pair q , respectively. We repeat (a,b) for setup 2 Model II in (c,d), respectively. We choose $q = 0.22$ for (a) and (c). We consider $J_A = 3.13$ for (b) and (d). Parameters: $t = 40 \text{ meV}$, $\mu_s = \mu_0 = -1.875t$, $\Delta_s = 0.0125t$, $\alpha = 0$, $L_l = L_r = L_{qw} = 20$.

of MCA. γ_I^1 behaves non-monotonically with λ . Importantly, intermediate (higher) value of J_A shows maximum efficiency for a relatively smaller (greater) value of λ . This indicates that there is a relative competition between SOC and AM for JDE to observe.

We continue the above analysis for Model II in Fig. 11. It is observed from Fig. 11 (a) that the ABS contribution to diode efficiency is higher than MCA. From Fig. 11 (b), we can conclude that close to 0.6 diode efficiency can be achieved for a relatively smaller value of J_A as compared to Model I. Importantly, a smaller region in $\Delta'_p/\Delta'_s - J_A$ plane shows significant efficiency which is attributed to the ABS contribution. This is in contrast to the Model I where ABS and MCA both lead to substantial efficiency in a broader region over $\Delta'_p/\Delta'_s - J_A$ plane. A key outcome from the Fig. 11 (c) is that the γ vanishes for values $\alpha = \pi/4, 3\pi/4$ while efficiency peaks around $\alpha = \pi/8, 3\pi/8, 5\pi/8$, and $7\pi/8$ for smaller value of J_A . This tendency persists for larger value of J_A as well, however, the efficiency is less. Importantly, for $\alpha = 0$, a

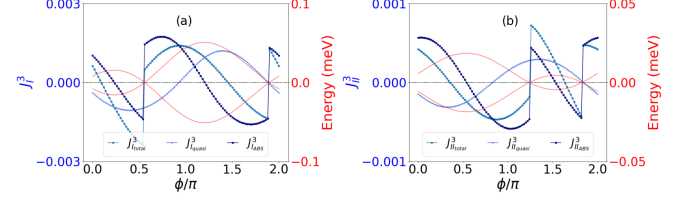


FIG. 14. We show the variation of supercurrent $J_I^3 \equiv J_{I_{\text{quasi}}}^3, J_{I_{\text{ABS}}}^3, J_{I_{\text{total}}}^3$ derived from Eqs. (13) and (14), and energy, with the superconducting phase difference (ϕ) for setup 3 Model I in (a). We repeat the same for setup 3 Model II in (b). We consider $J_A = 3.43$ for (a) and $J_A = 0.6565$ for (b). We choose $\alpha = 0$ for (a) and $\alpha = 0.48\pi$ for (b). Parameters: $t = 40 \text{ meV}$, $\mu_s = \mu_0 = -1.875t$, $\Delta_s = 0.0125t$, $\lambda = 0.05t$, $q = 0.34$, $L_l = L_r = L_{qw} = 20$.

single-component AM can not generate JDE in the presence of Rashba SOC and p -wave superconductivity. In Fig. 11 (d), we again show that JDE is absent when $J_A = 0 = \lambda$. The non-monotonic behavior in γ_{II}^1 with SOC is a common observation for both the models.

As discussed above in the context of Fig. 10 (c) and Fig. 11 (c) that at $\alpha = 0$ the diode efficiency is non-zero for Model I, while it is zero for Model II irrespective of the value of J_A . It can also be seen that once $\alpha \neq 0$ in Model II, we have non-zero diode efficiency. These observations are a direct signature of the JDE being only caused by the parallel spin components i.e., either by two-component AM or single-component AM in conjunction with Ising SOC, while the p -wave superconductivity is present. Note that the IS and TRS are broken in both of the above instances. This suggests that the crystallographic angle α can induce distinct tunability for the JD efficiency depending upon the nature of SOC. We note that the JDE was studied earlier with external magnetic field¹⁰³. Our work sheds light on the field-free JDE where JD efficiency can be controlled with J_A and α suggesting more tunability in the field-free case. However, the p -wave pairing is very important to obtain JDE even in the field-free case. Interestingly, the JD efficiency in AM-mediated case is significantly higher than the magnetic field-mediated case¹⁰³.

Setup 2: Having demonstrated the setup 1, we now turn our attention to the setup 2 for Model I and Model II in Figs. 12 and 13, respectively. We find ABS contributions in both the models give rise to JDE as shown in Figs. 12 (a), and 12 (b), however, finite-momentum does not cause significant non-reciprocity compared to the p -wave superconductivity. The efficiency $\gamma_{I,II}^2$ in both models show delta-function like spiky behavior with J_A see Figs. 13 (a,c). We find an extended region of q within which JD efficiency shows primary peak-dip and secondary oscillations, see Figs. 13 (b,d). Interestingly, efficiency reverses its sign with positive and negative q .

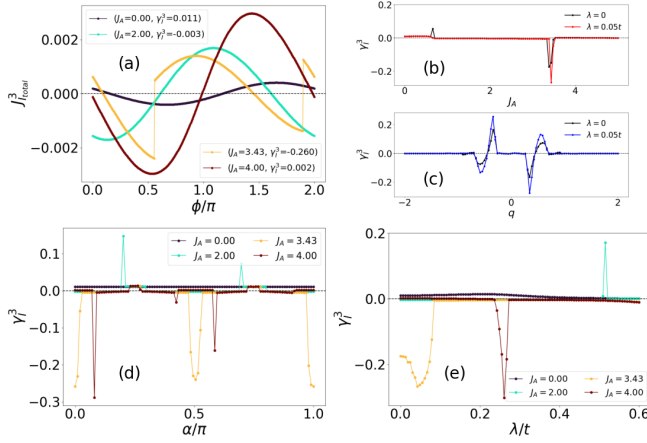


FIG. 15. In (a), we show the variation of supercurrent $J_{\text{I, total}}^3$, derived from Eq. (13) for setup 3 Model I, with the superconducting phase difference (ϕ). In (b,c), we illustrate the variation of γ_{I}^3 derived from Eq. (15) as a function of alter-magnet amplitude J_A , and the finite momentum of Cooper pair q , respectively. In (d,e), we display the variation of JD efficiency with α and Ising SOC λ , respectively. We consider $\lambda = 0.05t$ for (a) and (d). We consider $J_A = 3.43$ for (c). We choose $\alpha = 0$ for (a), (b), (c) and (e). We choose $q = 0.34$ for (a), (b), (d) and (e). Parameters: $t = 40$ meV, $\mu_s = \mu_0 = -1.875t$, $\Delta_s = 0.0125t$, $L_l = L_r = L_{qw} = 20$.

Importantly, JD efficiency is finite even for $J_A = 0$ and $\lambda = 0$ indicating the fact that finite momentum causes IS and TRS breaking that results in MCA. At the same time, this also renders the limitations of MCA with s -wave superconductivity when AM and SOC are both present in the quantum wire.

Setup 3: We first examine the dispersion and the associated Josephson current $J_{\text{I,II}}^3 \equiv J_{\text{I,II,quasi}}^3, J_{\text{I,II,ABS}}^3, J_{\text{I,II,total}}^3$ in Figs. 14 (a) and 14 (b) for Model I and II, respectively. We find that the quasi-contribution J_{quasi} does not show any non-reciprocity while J_{ABS} is the key resource for the non-reciprocity in $J_{\text{I,II,total}}^3$. The degree of non-reciprocity is more compared to case 2 advising the fact that the simultaneous presence of SOC, AM with FF superconductivity in the left superconductor suffices for JDE even in the absence of Δ_p type superconducting gap. Note that the left superconductor can show SDE as studied in the previous section can now host JDE when it is in contact with the quantum wire that only contains hopping. Therefore, MCA along with finite-momentum superconductivity can give rise to JDE under appropriate conditions.

We now turn our attention to the variation of current $J_{\text{I,II,total}}^3$ and efficiency $\gamma_{\text{I(II)}}^3$ with the angle α , SOC λ , AM strength J_A and finite momentum q for Model I and II in Figs. 15 and 16, respectively. The ABS contributions to non-reciprocal behavior of current changes as J_A changes for both models, see Fig. 15 (a) and Fig 16

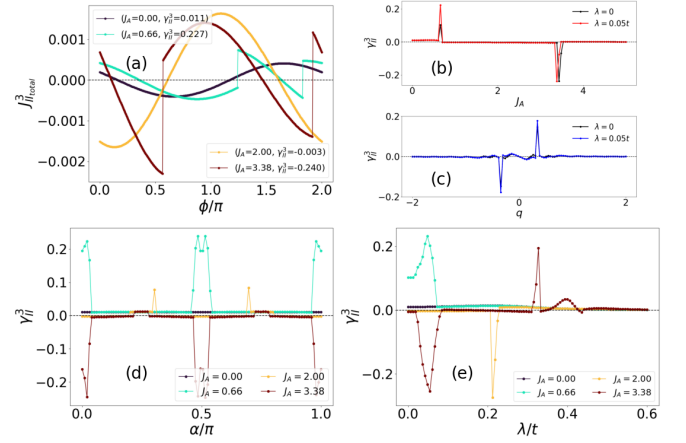


FIG. 16. In (a), we show the variation of supercurrent $J_{\text{II, total}}^3$, derived from Eq. (13) for setup 3 Model II, with the superconducting phase difference (ϕ). In (b,c), we illustrate the variation of γ_{II}^3 derived from Eq. (15) as a function of alter-magnet amplitude J_A , and the finite momentum of Cooper pair q , respectively. In (d,e), we display the variation of JD efficiency with α and Rashba SOC λ , respectively. We consider $\lambda = 0.05t$ for (a) and (d). We consider $J_A = 0.6565$ for (c). We choose $\alpha = 0.48\pi$ for (a), (b), (c) and (e). We choose $q = 0.34$ for (a), (b), (d) and (e). Parameters: $t = 40$ meV, $\mu_s = \mu_0 = -1.875t$, $\Delta_s = 0.0125t$, $L_l = L_r = L_{qw} = 20$.

(a). For some values of J_A , the ABS contribution is completely absent leading to vanishing non-reciprocity. This is markedly different from setup 1 where quasi contribution to Josephson current also shows significant non-reciprocity. Therefore, the MCA along with finite momentum in setup 3 is very effective in generating the non-reciprocity in the ABS contribution. We find an isolated value of J_A at which γ_{I}^3 shows a sharp dip, caused by the ABS contribution only, as displayed in Fig. 15 (b). There exists a window in q for which γ_{I}^3 remains finite, see Fig. 15 (c). This is similar to case 2, however, γ_{I}^3 shows prominent peaks and dips both in either sides of $q = 0$ referring to a smooth behavior of efficiency for case 3 as compared to case 2. Interestingly, the efficiency does not change its sign with α for a given value of J_A , see Fig. 15 (d). This is markedly different from setup 1 where α makes the efficiency alter its sign. The magnitude of efficiency increases with J_A as far as the peak or dip values of efficiency are considered. We find similar results when efficiency is examined with the strength of Ising SOC λ , see Fig. 15 (e). Importantly, efficiency is non-zero for $J_A = 0 = \lambda$ ensuring the presence of MCA for $q \neq 0$. The MCA-mediated non-reciprocity is indeed small while JDE here is mainly composed of ABS-mediated.

We now perform the same analysis for the Model II in Fig. 16. Rashba SOC works similar to Ising SOC to observe JDE. The non-reciprocity in $J_{\text{II, total}}^3$ is mainly governed by ABS, see Fig. 16 (a). We find two isolated values of J_A at which γ_{II}^3 shows sharp peak and dip, see

Fig. 16 (b). Efficiency displays a similar pattern with q in Fig. 16 (c). These features are distinct as compared to Model I as γ_{II}^3 shows high positive (negative) values for a certain positive (negative) q value in model I. Efficiency shows high positive and negative (only high negative) values for certain values of J_A in model II (I). The sign of efficiency does not change with α and λ for a given value of J_A , see Figs. 16 (d) and (e). There exist dissimilarities with respect to Model I as the maximum value of efficiency does not increase with J_A . Therefore, the nature of the SOC plays a significant role in optimizing the response within a given parameter window.

Upon investigating the three setups, we find that the efficiency is maximized when p -wave superconducting gap $\Delta'_p \neq 0$ is substantially high with respect to the s -wave superconducting gap Δ'_s . The efficiency $\gamma_{\text{I,II}}^1$ is found to be 60% which is greater than $\gamma_{\text{I,II}}^3 \sim 20\%$ where finite-momentum pairing is the key ingredient. Therefore, p -wave superconductivity is still found to be more efficient than finite momentum pairing. The reason could be attributed to the fact that JDE is caused by MCA and ABS in setup 1 while it is solely caused by ABS in setup 3. Nevertheless, setup 3 proves that p -wave pairing is not mandatory to observe JDE. ABS has a finite contribution towards non-reciprocity of critical current both in the presence and absence of p -wave pairing. The JDE requires breaking of IS and TRS thus leading to MCA while ABS is intrinsic in nature. In setup 1, the JDE is absent in the absence of AM and SOC. However, JDE is present in setup 1 when two parallel spin components are present i.e., either there exists two-component AM or single-component AM and Ising SOC are simultaneously present. This is in complete contrast to the setup 3 where JDE persists, with very little efficiency, even in the absence of AM and SOC. Interestingly, finite momentum breaks IS and TRS of the model generating an effective MCA. On the other hand, ABS causes the non-reciprocity when the parity of the mid-gap states switches. In the setup 3, the different types of SOC alters the behavior of efficiency with the remaining tuning parameter such as α , J_A . These changes in the behavior of efficiency are not very evident for setup 1 where p -wave superconductivity exists. Also, it can be seen that the sign of efficiency can be kept fixed using the FF-state of superconductivity.

IV. CONNECTION BETWEEN FIELD-FREE SDE AND JDE

In this section, we intend to find the underlying connection between the SDE and JDE. The MCA causes both the diode effects to appear. As we have shown, two-component AM with finite crystallographic angle can break both the symmetries and sufficing the role of a magnetic field and SOC. This is why SDE can be observed even in the absence of SOC in both Model I

and II. In other words, the simultaneous presence of a single-component AM and Ising SOC above a threshold strength could lead to SDE even in the absence of Rashba SOC. Interestingly, the above phenomena are mainly caused due to existence of parallel spin components with complementary momentum functions. Such an arrangement breaks TRS and IS at the same time. Interestingly, the same arrangement leads to the emergence of JDE in setup 1 in the presence of p -wave superconductivity where Rashba SOC is no longer required. Similarly, finite momentum of Cooper pair breaks TRS and IS both and results in MCA. This is why JDE is observed in setup 2 and 3 even in the absence of AM and SOC. However, the JD efficiency is significantly suppressed for setup 2 when the superconductor model does not host FF superconductivity, SOC and AM all simultaneously unlike setup 3 that exhibits noticeable JDE. Therefore, MCA is the regulator of the diode effects while the source of MCA can be external or internal. In our case, all the ingredients are primarily internal and hence SDE or JDE can be obtained while crystallographic angle and chemical potential can result in significant tunability. Moreover, the crystallographic angle plays a crucial role in terms of sign reversal of the efficiency. The variation of this angle can be understood as the lattice orientation with respect to its magnetic profile. In short, the parallel spin components with complementary momentum functions along with finite FF pairing are instrumental to experience the SDE in 1D. The above ingredients causes JDE to appear as well in 1D even in the absence of p -wave superconductivity.

V. CONCLUSION

In this work, we have proposed and analysed AM as a new and effective route to achieve nonreciprocal transport in superconductors. Traditionally, diode effects in superconductors have relied on external Zeeman fields, breaking TRS in conjunction with SOC that breaks IS. Our results demonstrate that AM can naturally fulfill this role, offering a field-free, tunable, and symmetry-driven pathway to realize the diode effect in a superconductor and in a Josephson junction namely, SDE and JDE, respectively. We consider a crystallographic angle in alter-magnetic term such that the diode effects can be studied with the strength of AM J_A as well as angle α .

We start with SDE in 1D where we consider Ising SOC and Rashba SOC to investigate the tunability of SD efficiency with parameters in Model I and II, respectively. The finite-momentum pairing of FF state is a prerequisite to experience SDE while integrating with the MCA. From the band structures of the low-energy BdG versions of the above models, we find that the gap of the inner and outer Fermi surface closing at different values of probe current is a direct indication of field-free SDE with AM. We find that the supercurrent changes its sign just once till the

maximum non-reciprocity is achieved while varying J_A for both the models. The variation of SD efficiency with chemical potential shows qualitatively similar features. Interestingly, the nature of the SOC nontrivially modifies their behavior with J_A and α . The sign of efficiency can be reversed by α irrespective of the nature of SOC while there exists SDE at $\alpha = 0$ above a threshold value of Ising SOC only. On the other hand, Rashba SOC can not mediate SDE for $\alpha = 0$. Importantly, SDE is found to survive in the absence of any SOC for certain windows of α as long as $J_A \neq 0$. This suggests that parallel spin components with complementary symmetry functions, either arising from a two-component altermagnetic (AM) order or from a combination of single-component AM and Ising spin-orbit coupling (SOC), can generate a superconducting diode effect (SDE) in the presence of finite-momentum pairing, provided that IS and TRS are simultaneously broken. Therefore, the AM alone with the help of finite crystallographic angle i.e., two-component AM can mediate SDE of high efficiency even in the absence of SOC. We also extend our analysis to tight-binding lattice model where we find qualitatively similar band gap closing, however, the efficiency is found to be small as compared to the low-energy models.

Having studied the SDE via the altermagnetic route, we continue to explore these models in the context of JDE in 1D, where three distinct setups are considered. AM allows us to investigate field-free JDE in the following setups. In setup 1 (2), we have p - and s -wave (FF) superconductors in contact with an intermediate quantum wire carrying Ising/ Rashba SOC and AM. In setup 3, we consider an FF superconductor with Ising/ Rashba SOC and AM, and an s -wave superconductor and both of them are in contact with the intermediate quantum wire containing hopping only. Interestingly, MCA is guaranteed by FF pairing, causing the JDE to appear in setups 2 and 3 irrespective of AM and SOC, while p -wave superconductivity in conjunction with AM causes a significant MCA to arise in setup 1, leading to a higher efficiency than that of setups 2 and 3. The quasi-contribution to the Josephson current from bulk bands can be attributed to the MCA while the ABS-contribution is caused by the states lying inside the s -wave superconducting gap. We find that JDE in setup 1 contains both quasi- as well as ABS-contributions while for setup 3 it is maximally dominated by ABS-contributions. This also engenders the efficiency in setup 1 to acquire high value as compared to setup 3. Similar to SDE, the parallel spin components with complementary momentum functions are also found to be responsible to secure JDE in the presence of p -wave superconductivity. Therefore, setup 1 shows the emergence of JDE in the absence of FF pairing while IS and TRS are broken by the the parallel spin components. Surprisingly, the JD efficiency in setup 2 is negligible as compared to that of setup 3. This is indicative of the fact

that the FF superconductor embedding the properties of the quantum wire namely, AM and SOC is more effective than a FF superconductor without having the above features. Note that the FF superconductor with AM and SOC is able to produce SDE and the same model can lead to JDE when a heterojunction with another s -wave superconductor and quantum wire without AM and SOC is made to form a Josephson junction. Importantly, the sign of efficiency changes with the crystallographic angle in setup 1 with p -wave superconductivity while such sign reversal is completely absent for setup 3. Therefore, in terms of JD efficiency p -wave superconductivity is more relevant even in the field-free case. On the other hand, FF superconductivity produces ABS-driven JDE with contrasting angle-dependencies.

Overall, our findings highlight altermagnet-superconductor hybrids as ideal candidates for realizing efficient, magnet-free superconducting diodes in 1D. Such systems combine microscopic tunability, material flexibility, and robustness against external perturbations, making them promising for future quantum technologies requiring directional supercurrents. Moreover, the coexistence of SDE and JDE mechanisms uncovered here points toward a unified picture of nonreciprocal superconductivity where finite-momentum pairing, ABS, and band asymmetry act together to produce robust diode behaviour in 1D. Looking ahead, our work lays a foundation for future experimental exploration of altermagnetic materials integrated with superconductors. Investigating multi-band effects, thermal influences, non-Hermitian systems, time-driven systems and topological extensions of these systems could further enrich our understanding of non-reciprocity in unconventional superconductors, and perhaps lead to the realization of tunable quantum rectifiers operating in realistic devices. The interplay of Rashba SOC and AM can induce nontrivial topological features in an underlying s -wave superconductor, thereby opening a route to topological SDE and JDE where the coexistence of Ising SOC, Rashba SOC, and AM in a FF superconductor facilitates the above.

VI. ACKNOWLEDGMENT

We thank Arijit Saha and Sayak Bhoumik for useful discussions. TN thanks NFSG “NFSG/HYD/2023/H0911” from BITS Pilani.

REFERENCES

* tanay.nag@hyderabad.bits-pilani.ac.in

¹ J. Bardeen, L. N. Cooper, and J. R. Schrieffer, Phys. Rev. **108**, 1175 (1957).

² F. Ando, Y. Miyasaka, T. Li, J. Ishizuka, T. Arakawa, Y. Shiota, T. Moriyama, Y. Yanase, and T. Ono, Nature **584**, 373 (2020).

³ G. Takeuchi and M. Eto, Journal of the Physical Society of Japan **94**, 054701 (2025).

⁴ T. Zhou, W.-S. Du, W.-H. Wang, Q. Yang, H.-D. Miao, Y. Zhou, Z. Zhang, Y. Zhao, H. Jia, S. Liu, *et al.*, Nanoscale **17**, 5888 (2025).

⁵ S. Chahid, S. Teknowijoyo, I. Mowgood, and A. Gulian, Phys. Rev. B **107**, 054506 (2023).

⁶ Y.-Y. Lyu, J. Jiang, Y.-L. Wang, Z.-L. Xiao, S. Dong, Q.-H. Chen, M. V. Milošević, H. Wang, R. Divan, J. E. Pearson, *et al.*, Nature communications **12**, 2703 (2021).

⁷ Y. Hou, F. Nichele, H. Chi, A. Lodesani, Y. Wu, M. F. Ritter, D. Z. Haxell, M. Davydova, S. Ilić, O. Glezakou-Elbert, A. Varambally, F. S. Bergeret, A. Kamra, L. Fu, P. A. Lee, and J. S. Moodera, Phys. Rev. Lett. **131**, 027001 (2023).

⁸ D. Li, Z. Lu, W. Cheng, X. Shi, L. Hu, X. Ma, Y. Liu, Y. M. Itahashi, T. Shitaokoshi, P. Li, *et al.*, Communications Physics **8**, 70 (2025).

⁹ U. Nagata, M. Aoki, A. Daido, S. Kasahara, Y. Kasahara, R. Ohshima, Y. Ando, Y. Yanase, Y. Matsuda, and M. Shiraishi, Phys. Rev. Lett. **134**, 236703 (2025).

¹⁰ S. Qi, J. Ge, C. Ji, Y. Ai, G. Ma, Z. Wang, Z. Cui, Y. Liu, Z. Wang, and J. Wang, Nature Communications **16**, 531 (2025).

¹¹ P. Fulde and R. A. Ferrell, Phys. Rev. **135**, A550 (1964).

¹² Y. Matsuda and H. Shimahara, Journal of the Physical Society of Japan **76**, 051005 (2007).

¹³ A. B. Vorontsov, J. A. Sauls, and M. J. Graf, Phys. Rev. B **72**, 184501 (2005).

¹⁴ M. Ichioka, H. Adachi, T. Mizushima, and K. Machida, Phys. Rev. B **76**, 014503 (2007).

¹⁵ R. Lortz, Y. Wang, A. Demuer, P. H. M. Böttger, B. Bergk, G. Zwicknagl, Y. Nakazawa, and J. Wosnitza, Phys. Rev. Lett. **99**, 187002 (2007).

¹⁶ Q. Cui, C.-R. Hu, J. Y. T. Wei, and K. Yang, Phys. Rev. B **73**, 214514 (2006).

¹⁷ C. Qu, Z. Zheng, M. Gong, Y. Xu, L. Mao, X. Zou, G. Guo, and C. Zhang, Nature communications **4**, 2710 (2013).

¹⁸ W. Zhang and W. Yi, Nature communications **4**, 2711 (2013).

¹⁹ N. F. Yuan and L. Fu, Proceedings of the National Academy of Sciences **118**, e2019063118 (2021).

²⁰ Y. Yuan and L. Fu, Proc. Natl. Acad. Sci. U.S.A. **119**, e2119548119 (2022).

²¹ F. Ando, Y. Miyasaka, T. Li, J. Ishizuka, T. Arakawa, Y. Shiota, T. Moriyama, D. Chiba, F. Matsukura, T. Ono, and H. Ohno, Nature **584**, 373 (2020).

²² C. Legg, D. Loss, and J. Klinovaja, Phys. Rev. B **106**, 104501 (2022).

²³ A. Daido, Y. Ikeda, and Y. Yanase, Phys. Rev. Lett. **128**, 037001 (2022).

²⁴ A. Daido and Y. Yanase, Phys. Rev. B **106**, 205206 (2022).

²⁵ K. Nakamura, A. Daido, and Y. Yanase, Phys. Rev. B **109**, 094501 (2024).

²⁶ D. Chakraborty and A. M. Black-Schaffer, Phys. Rev. Lett. **135**, 026001 (2025).

²⁷ S. Bhowmik, D. Samanta, A. K. Nandy, A. Saha, and S. K. Ghosh, Communications Physics **8**, 260 (2025).

²⁸ S. Bhowmik and A. Saha, Phys. Rev. B **111**, L161402 (2025).

²⁹ J. Ma, R. Zhan, and X. Lin, Advanced Physics Research **1**, 2400180 (2025).

³⁰ M. Nadeem, M. S. Fuhrer, and X. Wang, Nature Reviews Physics **5**, 558 (2023).

³¹ J. Hasan, D. Shaffer, M. Khodas, and A. Levchenko, Phys. Rev. B **111**, 174514 (2025).

³² G. Angehrn, H. F. Legg, D. Loss, and J. Klinovaja, Applied Physics Letters **125** (2024).

³³ Y. Tanaka, B. Lu, and N. Nagaosa, Phys. Rev. B **106**, 214524 (2022).

³⁴ J. J. He, Y. Tanaka, and N. Nagaosa, New Journal of Physics **24**, 053014 (2022).

³⁵ T. Karabassov, E. S. Amirov, I. V. Bobkova, A. A. Golubov, E. A. Kazakova, and A. S. Vasenko, Condensed Matter **8**, 36 (2023).

³⁶ J. Hasan, D. Shaffer, M. Khodas, and A. Levchenko, Phys. Rev. B **110**, 024508 (2024).

³⁷ G. L. J. A. Rikken, J. Fölling, and P. Wyder, Phys. Rev. Lett. **87**, 236602 (2001).

³⁸ T. Yokouchi, Y. Ikeda, T. Morimoto, and Y. Shiomi, Phys. Rev. Lett. **130**, 136301 (2023).

³⁹ G. L. J. A. Rikken and N. Avarvari, Phys. Rev. B **99**, 245153 (2019).

⁴⁰ D. Mondal, A. Pal, A. Saha, and T. Nag, Phys. Rev. B **111**, L121401 (2025).

⁴¹ D. Mondal, A. K. Ghosh, T. Nag, and A. Saha, Phys. Rev. B **107**, 035427 (2023).

⁴² J. Ingla-Aynés, Y. Hou, S. Wang, E.-D. Chu, O. A. Mukhanov, P. Wei, and J. S. Moodera, Nature Electronics **1**, 1 (2025).

⁴³ W. Yu, J. J. Cuozzo, K. Sapkota, E. Rossi, D. X. Rademacher, T. M. Nenoff, and W. Pan, Phys. Rev. B **110**, 104510 (2024).

⁴⁴ B. Turini, S. Salimian, M. Carrega, A. Iorio, E. Strambini, F. Giazotto, V. Zannier, L. Sorba, and S. Heun, Nano Letters **22**, 8502 (2022).

⁴⁵ M. Trahms, L. Melischeck, J. F. Steiner, B. Mahendru, I. Tamir, N. Bogdanoff, O. Peters, G. Reecht, C. B. Winkelmann, F. von Oppen, *et al.*, Nature **615**, 628 (2023).

⁴⁶ M. Coraiola, A. E. Svetogorov, D. Z. Haxell, D. Sabonis, M. Hinderling, S. C. Ten Kate, E. Cheah, F. Krizek, R. Schott, W. Wegscheider, *et al.*, ACS nano **18**, 9221 (2024).

⁴⁷ Y.-M. Gao, H. Xiao, M.-H. Jiang, F. Chi, Z.-C. Yi, and L.-M. Liu, Nanomaterials **14**, 1251 (2024).

⁴⁸ H. Wu, Y. Wang, Y. Xu, P. K. Sivakumar, C. Pasco, U. Filippozzi, S. S. Parkin, Y.-J. Zeng, T. McQueen, and M. N. Ali, Nature **604**, 653 (2022).

⁴⁹ H. Wu, Y. Wang, Y. Xu, P. K. Sivakumar, C. Pasco, U. Filippozzi, S. S. Parkin, Y.-J. Zeng, T. McQueen, and M. N. Ali, arXiv preprint arXiv:2103.15809 (2021).

⁵⁰ M. Davydova, S. Prembabu, and L. Fu, *Science advances* **8**, eab0309 (2022).

⁵¹ B. Pal, A. Chakraborty, P. K. Sivakumar, M. Davydova, A. K. Gopi, A. K. Pandeya, J. A. Krieger, Y. Zhang, M. Date, S. Ju, *et al.*, *Nature physics* **18**, 1228 (2022).

⁵² Y. Zhang, Y. Gu, P. Li, J. Hu, and K. Jiang, *Phys. Rev. X* **12**, 041013 (2022).

⁵³ R. S. Souto, M. Leijnse, and C. Schrade, *Phys. Rev. Lett.* **129**, 267702 (2022).

⁵⁴ S. Matsuo, T. Imoto, T. Yokoyama, Y. Sato, T. Linde-mann, S. Gronin, G. C. Gardner, M. J. Manfra, and S. Tarucha, *Nature Physics* **19**, 1636 (2023).

⁵⁵ A. Zazunov, J. Rech, T. Jonckheere, B. Grémaud, T. Martin, and R. Egger, *Physical Review B* **109**, 024504 (2024).

⁵⁶ J.-X. Hu, Z.-T. Sun, Y.-M. Xie, and K. T. Law, *Phys. Rev. Lett.* **130**, 266003 (2023).

⁵⁷ A. Soori, *Physica Scripta* **98**, 065917 (2023).

⁵⁸ P. A. Volkov, E. Lantagne-Hurtubise, T. Tummuru, S. Plugge, J. H. Pixley, and M. Franz, *Phys. Rev. B* **109**, 094518 (2024).

⁵⁹ G.-Q. Wang, J.-J. Miao, and W.-Q. Chen, *Phys. Rev. B* **112**, 014508 (2025).

⁶⁰ D. Debnath and P. Dutta, *Phys. Rev. B* **109**, 174511 (2024).

⁶¹ M. Mori, W. Koshibae, and S. Maekawa, *arXiv preprint arXiv:2501.05671* (2025).

⁶² A. Boruah, S. Acharjee, and P. K. Saikia, *Phys. Rev. B* **112**, 054505 (2025).

⁶³ J.-D. Pillet, S. Annabi, A. Peugeot, H. Riechert, E. Arriighi, J. Griesmar, and L. Bretheau, *Phys. Rev. Res.* **5**, 033199 (2023).

⁶⁴ J. L. Huamani Correa and M. P. Nowak, *SciPost Physics* **17**, 037 (2024).

⁶⁵ A. Maiellaro, M. Trama, J. Settino, C. Guarcello, F. Romeo, and R. Citro, *SciPost Physics* **17**, 101 (2024).

⁶⁶ N. F. Yuan and L. Fu, *Proceedings of the National Academy of Sciences* **119**, e2119548119 (2022).

⁶⁷ A. Bordin, F. J. Bennebroek Everts, G. O. Steffensen, T. Dvir, G. P. Mazur, D. van Driel, N. van Loo, J. C. Wolff, E. P. A. M. Bakkers, A. L. Yeyati, and L. P. Kouwenhoven, *Phys. Rev. X* **15**, 011046 (2025).

⁶⁸ S. Mondal, P.-H. Fu, and J. Cayao, *Phys. Rev. B* **112**, 144506 (2025).

⁶⁹ L. Bauriedl, C. Bäuml, L. Fuchs, C. Baumgartner, N. Paulik, J. M. Bauer, K.-Q. Lin, J. M. Lupton, T. Taniguchi, K. Watanabe, *et al.*, *Nature communications* **13**, 4266 (2022).

⁷⁰ B. Lu, S. Ikegaya, P. Burset, Y. Tanaka, and N. Nagaosa, *Phys. Rev. Lett.* **131**, 096001 (2023).

⁷¹ K. Chen, B. Karki, and P. Hosur, *Phys. Rev. B* **109**, 064511 (2024).

⁷² J. Cayao, N. Nagaosa, and Y. Tanaka, *Phys. Rev. B* **109**, L081405 (2024).

⁷³ Z. Liu, L. Huang, and J. Wang, *Phys. Rev. B* **110**, 014519 (2024).

⁷⁴ L. Šmejkal, J. Sinova, and T. Jungwirth, *Phys. Rev. X* **12**, 031042 (2022).

⁷⁵ L. Šmejkal, J. Sinova, and T. Jungwirth, *Phys. Rev. X* **12**, 031042 (2022).

⁷⁶ S. Reimers, L. Odenbreit, L. Šmejkal, V. N. Strocov, P. Constantinou, A. B. Hellenes, R. Jaeschke Ubiergo, W. H. Campos, V. K. Bharadwaj, A. Chakraborty, *et al.*, *Nature Communications* **15**, 2116 (2024).

⁷⁷ J. Ding, Z. Jiang, X. Chen, Z. Tao, Z. Liu, T. Li, J. Liu, J. Sun, J. Cheng, J. Liu, *et al.*, *Physical Review Letters* **133**, 206401 (2024).

⁷⁸ G. Yang, Z. Li, S. Yang, J. Li, H. Zheng, W. Zhu, Z. Pan, Y. Xu, S. Cao, W. Zhao, *et al.*, *Nature Communications* **16**, 1442 (2025).

⁷⁹ R. Tamang, S. Gurung, D. P. Rai, S. Brahimi, and S. Lounis, *Magnetism* **5**, 17 (2025).

⁸⁰ S.-W. Cheong and F.-T. Huang, *npj Quantum Materials* **10**, 38 (2025).

⁸¹ I. Mazin (The PRX Editors), *Phys. Rev. X* **12**, 040002 (2022).

⁸² R. Tamang, S. Gurung, D. Rai, S. Brahimi, and S. Lounis, *arXiv preprint arXiv:2412.05377* (2024).

⁸³ L. Šmejkal, J. Sinova, and T. Jungwirth, *Phys. Rev. X* **12**, 040501 (2022).

⁸⁴ S. Bhowal and N. A. Spaldin, *Phys. Rev. X* **14**, 011019 (2024).

⁸⁵ S.-W. Cheong and F.-T. Huang, *npj Quantum Materials* **9**, 13 (2024).

⁸⁶ P. Chatterjee and V. Jurić, *Phys. Rev. B* **112**, 054503 (2025).

⁸⁷ D. Zhu, Z.-Y. Zhuang, Z. Wu, and Z. Yan, *Phys. Rev. B* **108**, 184505 (2023).

⁸⁸ S. A. A. Ghorashi, T. L. Hughes, and J. Cano, *Phys. Rev. Lett.* **133**, 106601 (2024).

⁸⁹ D. Chakraborty and A. M. Black-Schaffer, *Phys. Rev. B* **112**, 014516 (2025).

⁹⁰ P. O. Sukhachov, E. W. Hodt, and J. Linder, *Phys. Rev. B* **110**, 094508 (2024).

⁹¹ M. Papaj, *Phys. Rev. B* **108**, L060508 (2023).

⁹² B. Lu, K. Maeda, H. Ito, K. Yada, and Y. Tanaka, *Phys. Rev. Lett.* **133**, 226002 (2024).

⁹³ C. Li, M. Hu, Z. Li, Y. Wang, W. Chen, B. Thiagarajan, M. Leandersson, C. Polley, T. Kim, H. Liu, C. Fulga, M. G. Vergniory, O. Janson, O. Tjernberg, and J. van den Brink, *Communications Physics* **8**, 311 (2025).

⁹⁴ S. Liu, Z. Zhang, L. Bai, and W. Feng, *Phys. Rev. B* **111**, 184437 (2025).

⁹⁵ R. González-Hernández, H. Serrano, and B. Uribe, *Phys. Rev. B* **111**, 085127 (2025).

⁹⁶ Z. Li, Z. Li, and Z. Qiao, *Phys. Rev. B* **111**, 155303 (2025).

⁹⁷ P. Dong, J. Wang, Y. Wang, J. Xiao, X. Zhou, H. Xing, Y. Wu, Y. Chen, J. Wen, and J. Li, *arXiv preprint arXiv:2510.00575* (2025).

⁹⁸ S. Li, Y. Deng, D. Hu, C. Zhu, Z. Yang, W. Tian, X. Wang, M. Yue, Q. Wu, Z. Liu, *et al.*, *ACS nano* **18**, 31076 (2024).

⁹⁹ D. Samanta and S. K. Ghosh, *arXiv preprint arXiv:2507.21446* (2025).

¹⁰⁰ Q. Cheng, Y. Mao, and Q.-F. Sun, *Phys. Rev. B* **110**, 014518 (2024).

¹⁰¹ H. Vakili, M. Ali, and A. A. Kovalev, *Phys. Rev. B* **110**, 104518 (2024).

¹⁰² L. Sharma and M. Thakurathi, *Phys. Rev. B* **112**, 104506 (2025).

¹⁰³ A. Soori, *Journal of Physics: Condensed Matter* **37**, 10LT02 (2025), *arXiv:2409.02794* [cond-mat.supr-con].

¹⁰⁴ T. de Picoli, Z. Blood, Y. Lyanda-Geller, and J. I. Väyrynen, *Phys. Rev. B* **107**, 224518 (2023).

¹⁰⁵ S. Bhowmik, D. Samanta, A. K. Nandy, A. Saha, and S. K. Ghosh, *arXiv preprint arXiv:2508.10832* (2025).

¹⁰⁶ R. Hess, H. F. Legg, D. Loss, and J. Klinovaja, Phys. Rev. B **108**, 174516 (2023).

¹⁰⁷ A. Daido, Y. Ikeda, and Y. Yanase, Phys. Rev. Lett. **128**, 037001 (2022).

¹⁰⁸ J. J. Kinnunen, J. E. Baarsma, J.-P. Martikainen, and P. Törmä, Rep. Prog. Phys. **81**, 046401 (2018).

¹⁰⁹ M. V. Davydova, M. A. Silaev, T. T. Heikkilä, and F. S. Bergeret, Physical Review Letters **128**, 107001 (2022).

¹¹⁰ X. Liu, J.-J. Lee, and A. V. Chubukov, Physical Review B **110**, 144501 (2024).